Nonunitary triplet superconductivity tuned by field-controlled magnetization: URhGe, UCoGe, and UTe_2

Kazushige Machida
Department of Physics, Ritsumeikan University, Kusatsu 525-8577, Japan

(Received 19 January 2021; revised 31 May 2021; accepted 6 July 2021; published 20 July 2021)

We report on a theoretical study on ferromagnetic superconductors URhGe and UCoGe and identify the pairing state as a nonunitary spin-triplet one with time-reversal symmetry broken, analogous to the superfluid ^{3}He-*A* phase. A recently found superconductor UTe_2 with almost ferromagnetism is analyzed by the same manner. Through investigating their peculiar upper critical field H_{c2} shapes, it is shown that the pairing symmetry realized in all three compounds can be tuned by their magnetization curves under applied fields. This leads to the reentrant H_{c2} in URhGe, an S-shaped in UCoGe and an L-shaped H_{c2} in UTe_2 observed for the magnetic hard *b*-axis direction. The identification with double chiral form $\mathbf{d}(k) = (\hat{b} + i\hat{c})(k_b + ik_c)$ in UTe_2 naturally enables us to understand (1) multiple phases with A_1, A_2, and A_0 phases observed under pressure, (2) the enhanced reentrant H_{c2} for the off-axis direction associated with first-order metamagnetic transition, and (3) Weyl point nodes oriented along the magnetic easy *a* axis. All three compounds are found to be topologically rich solid-state materials worth further investigation.

DOI: 10.1103/PhysRevB.104.014514

I. INTRODUCTION

The competing orders are at the heart of the strongly correlated systems in general where multiple long- or short-range orderings, such as superconductivity (SC), ferromagnetism (FM), spin, and charge density waves are emerging out of the strong interactions in condensed matter systems. This is particularly true in the case of unconventional superconductivity, which is often associated with other orderings mentioned [1–3]. A good example is high-temperature cuprate superconductors in which various coexisting or mutually repulsive orderings are found [4].

There has been much attention focused on ferromagnetic superconductors [5], such as UGe_2 [6], URhGe [7], and UCoGe [8] in recent years. A new member of such a superconductor, UTe_2, whose $T_c = 1.6$ K [9,10], with ferromagnetic fluctuations is discovered quite recently and attracts much excitement. Those systems are contrasted with the coexisting materials of magnetism and superconductivity in $(RE)Rh_4B_4$ (RE: $4f$ rare-earth elements) and Chevrel compounds $(RE)Mo_6S_8$ in that the $4f$ electrons responsible for magnetism are localized spatially and distinctive from the conduction electrons [11]. Here the $5f$ electrons responsible for magnetism are more subtle in that they participate in both magnetism and superconductivity.

UTe_2 has been investigated experimentally [12–29] and theoretically [30–38]. Simultaneously, renewed interest on the former three compounds is developing. These heavy-fermion materials belong to a strongly correlated system that is heavily governed by the $5f$ electrons, which form a coherent narrow band with a large mass enhancement below the Kondo temperature. Because the upper critical field H_{c2} in those compounds exceeds the Pauli paramagnetic limitation, a spin triplet or odd parity pairing state is expected to be realized [5]. However, detailed studies of the pairing symmetry remain lacking despite the fact that previous knowledge of the first three compounds is accumulated for over two decades. Thus, now it is a good chance to understand those "old" materials URhGe and UCoGe together with the new UTe_2 by seeking some common features.

The prominent SC properties observed commonly in these superconductors are as follows: When H is applied parallel to the magnetic hard *b* axis in orthorhombic crystals, H_{c2} exhibits the reentrant behavior in URhGe, where the SC state that disappeared reappears at higher fields [39], or an S shape in UCoGe [40] and an L shape in UTe_2 [12] in the H-T plane. Above the superconducting transition temperature T_c, ferromagnetic transition occurs in URhGe and UCoGe. Thus, the SC state survives under a strong internal field, resulting from an exchange interaction between the conduction and the $5f$ electrons. However, in UTe_2 "static" FM has not been detected although FM fluctuations are probed [9,14,18,19] above T_c, i.e., there is a diverging static susceptibility along the magnetic easy *a* axis [9,14] and the nuclear relaxation time $1/T_2$ in nuclear magnetic resonance (NMR) [18].

The gap structure is unconventional, characterized by either a point in UTe_2 [9,10] or line nodes in the others [5]. There is clear experimental evidence for double transitions: The two successive second-order SC phase transitions seen in specific-heat experiments as distinctive jumps systematically change under pressure (P) in UTe_2 [13]. A similar indication for double SC transitions in ambient pressure is observed in UCoGe at $T_{c2} \sim 0.2$ K [41,42] where the nuclear relaxation time $1/T_1T$ in NMR experiments exhibits a plateau corresponding to the "half-residual density of states (DOS)" value at the intermediate T below $T_c = 0.5$ K. Upon further

lowering of T, it starts decreasing again at 0.2 K. Recent specific-heat C/T data for several high-quality samples of UTe_2 [9,10,29] commonly show the residual DOS amounting to $0.5N(0)$, which is half of the normal DOS $N(0)$, while some exhibit zero residual DOS [16]. Thus, this "residual" half DOS issue is currently controversial. We propose a method to resolve this issue, discussed later in this paper.

To understand these three spin-polarized superconductors URhGe, UCoGe, and UTe_2 in a unified way, we develop a phenomenological theory based on the assumption that the three compounds are coherently described in terms of the triplet pairing symmetry analogous to the superfluid ^{3}He-A phase [43]. It is instructive to remember that the A_1-A_2 phase transition is induced by an applied field, which is observed as the clear double specific-heat jumps [44]. The originally degenerate transition temperatures for the A phase are split into the A_1 and A_2 phases under applied fields [45].

Therefore, to address those experimental facts, we postulate the A-phase-like triplet pair symmetry, which responds to the spontaneous FM and/or induced moment under perpendicular external fields, to yield the A_1-A_2 double transitions. This scenario coherently explains the observed reentrant H_{c2} in URhGe, the S shape in UCoGe, and the L shape in UTe_2 for the field direction along the magnetic hard b axis in a unified way.

The A_1-A_2 phase transition in the ^{3}He-A phase [44] is controlled by the linear Zeeman effect due to the applied field which acts to split T_c [45]. In the spin-polarized superconductors T_c is controlled by the spontaneous and/or field-induced magnetic moment, which is linearly coupled to the nonunitary order parameter. We employ the Ginzburg-Landau (GL) theory to describe these characteristic H_{c2} curves. We also identify the pairing symmetry by group-theoretic classification [46] based on our previous method [47,48]. The pairing symmetry is a nonunitary triplet [46,49,50], where the **d** vector is a complex function that points perpendicular to the magnetic easy axis in zero field. The gap function possesses either a point or line node with a possibly chiral p-wave orbital form. This is maximally consistent with the SC characteristics obtained so far in UTe_2, such as the STM observation [17] of chiral edge states, the polar Kerr experiment [21], which shows time-reversal symmetry breaking, and other various thermodynamic measurements. We note that the realization of a nonunitary triplet pairing is discussed in connection with $LaNiGa_2$ [51].

The arrangement of this paper is following. We set up the theoretical framework to explain those experimental facts in the three compounds URhGe, UCoGe, and UTe_2 in Sec. II. The theory is based on the Ginzburg-Landau theory for the order parameter with three components. The quasiparticle spectra in the triplet states are examined to understand thermodynamic behaviors for the materials. In Sec. III we investigate the generic phase transitions of the present pairing state under fields applied to various field directions relative to the orthorhombic crystalline axes. In order to analyze the experimental data for URhGe, UCoGe, and UTe_2 which exhibit a variety of the H_{c2} such as reentrant SC (RSC), S-shaped, and L-shaped one, the magnetization curves for three compounds are studied in detail and the curves evaluated when the experimental data are absent in Sec. IV. We apply the present theory to the three compounds and explain the peculiar H_{c2} curves observed in Sec. V, including the multiple phase diagrams in UTe_2 under pressure. Section VI devotes to detailed discussions on the gap structure, and the pairing symmetries for each material. A summary and conclusion are given in the final Sec. VII. Throughout the paper we assume that the magnetism is uniform. The roles of magnetic inhomogeneity may become important, but it is beyond the scope of the paper. Here we assume that magnetism is homogeneous. This paper is a full paper version of the two short papers by the author [52,53].

The main differences of this version from the previous brief papers lie in the following aspects:

(1) In the present version we substantiate the basic ideas only briefly described in the previous papers by explicitly utilizing the magnetization curves in order to reproduce the characteristic H_{c2} shapes. The magnetization curves are taken from experimental data when available, or accurately evaluated theoretically when unavailable.

(2) In the previous papers we only discussed the H_{c2} curves for the magnetic easy axis. Here we cover not only three principal axes, a, b, and c axes in orthorhombic crystals, but also the angles between them. It will turn out that this is important because those provide us clean theoretical testing grounds without changing the material environments, such as impurities or alloying, etc., maintaining the same condition.

(3) Here we try to exhaust the available experimental data as possible as we can while in the previous ones it is limited and quite sketchy. Thus, we convince ourselves that the present version is consistent with experiments.

(4) Since this research field is rapidly evolving, we take into account recent experimental progresses after the publications of the two papers to sharpen our theory. This includes a remarkable observation of the **d**-vector rotation seen by the Knight shift experiments [54,55] on UTe_2, which precisely agrees with the prediction made in the present version.

(5) Through those detailed and exhaustive analyses we are now able to precisely pin down the pairing symmetries realized in all three compounds, in particular UTe_2, and furnish various predictions to further check our scenario.

II. THEORETICAL FRAMEWORK

A. Ginzburg-Landau theory

In order to understand a variety of experimental phenomena exhibited by the three compounds in a common theoretical framework, we start with the most generic Ginzburg-Landau (GL) theory for a spin-triplet state. This is general enough to allow us to describe the diversity of those systems. Among abundant spin-triplet or odd-parity paring states we assume an A-phase-like pairing state described by the complex **d** vector with three components:

$$\mathbf{d}(k) = \phi(k)\vec{\eta} = \phi(k)(\vec{\eta}' + i\vec{\eta}''). \tag{1}$$

$\vec{\eta}'$ and $\vec{\eta}''$ are real three-dimensional vectors in the spin space for Cooper pairs, and $\phi(k)$ is the orbital part of the pairing function. This is classified group theoretically under the overall symmetry:

$$\mathrm{SO}(3)_{\mathrm{spin}} \times D_{2h}^{\mathrm{orbital}} \times \mathrm{U}(1) \tag{2}$$

with the spin, orbital, and gauge symmetry, respectively [46,56].

In this study, we adopt the weak spin-orbit coupling scheme [47,48] which covers the strong spin-orbit coupling (SOC) case as a limit. The strength of the SOC depends on materials and is to be appropriately tuned relative to the experimental situations. It will turn out to be crucial to choose the weak SOC case in understanding the H_{c2} phase diagrams with peculiar shapes: This allows the **d**-vector rotation under an applied field whose strength is determined by the SOC. Note that in the strong SOC scheme the **d**-vector rotation field is infinite because the Cooper pair spin is locked to crystal lattices.

There exists U(1)×Z_2 symmetry in this pairing, i.e., invariance under $\mathbf{d} \to -\mathbf{d}$ and gauge transformations. We emphasize here that this SO(3) triple spin symmetry of the pairing function is expressed by a complex three-component vectorial order parameter $\vec{\eta} = (\eta_x, \eta_y, \eta_z)$ in the most general case. It will turn out later to be important also to describe complex multiple phase diagrams, consisting of five distinctive phases, but this is a minimal framework which is necessary and sufficient.

Under the overall symmetry expressed by Eq. (2), the most general Ginzburg-Landau free-energy functional up to the quadratic order is written as

$$F^{(2)} = \alpha_0(T - T_{c0})\vec{\eta}\cdot\vec{\eta}^\star + b|\vec{M}\cdot\vec{\eta}|^2 + cM^2\vec{\eta}\cdot\vec{\eta}^\star + i\kappa\vec{M}\cdot\vec{\eta}\times\vec{\eta}^\star \tag{3}$$

with b and c positive constants. The last invariant with the coefficient κ comes from the nonunitarity of the pairing function in the presence of the spontaneous moment and field induced $\vec{M}(H)$, which are to break the SO(3) spin-space symmetry in Eq. (2). We take $\kappa > 0$ without loss of generality. This term responds to external field directions differently through their magnetization curves. Here we neglect explicit magnetic field effect by assuming that it comes through $M(H)$. Thus, upon increasing H, the **d** vector can rotate when the magnetization direction changes so to maximally gain this term. It will turn out that this **d**-vector rotation is a key to understanding the peculiar H_{c2} curves.

The magnetic coupling κ, which is a key parameter to characterize materials of interest in the following, is estimated [45] by

$$\kappa = T_c\frac{N'(0)}{N(0)}\ln(1.14\omega/T_c), \tag{4}$$

where $N'(0)$ is the energy derivative of the normal density of states $N(0)$ at the Fermi level and ω is the energy cutoff. This term arises from the electron-hole asymmetry near the Fermi level. κ indicates the degree of this asymmetry, which can be substantial for a narrow band. Thus, the Kondo coherent band in heavy-fermion materials, such as in our case, is expected to be important. We can estimate $N'(0)/N(0) \sim 1/E_F$ with the Fermi energy E_F. Because $T_c = 2$ mK and $E_F = 1$ K in superfluid ^{3}He, $\kappa \sim 10^{-3}$. In the present compounds $T_c \sim 1$ K and $E_F \sim T_K$ with the T_K Kondo temperature being typically [5] 10 ∼ 50 K. Thus, κ is much larger than that of superfluid ^{3}He and is an order of $1 \sim 10^{-1}$. We will assign the κ value for each compound to reproduce the phase diagram in the following as tabulated in Table I.

TABLE I. Magnetic properties and κ values.

Materials	Curie temp. (K)	Easy axis	Moment (μ_B)	κ (K/μ_B)
URhGe	9.5	c axis	$M_c = 0.4$	2.0
UCoGe	2.5	c axis	$M_c = 0.06$	1.8
UTe_2		a axis	$\sqrt{\langle M_a^2\rangle} = 0.48$	6.9

The fourth-order term in the GL functional is given by [46,56]

$$F^{(4)} = \frac{\beta_1}{2}(\vec{\eta}\cdot\vec{\eta}^\star)^2 + \frac{\beta_2}{2}|\vec{\eta}^2|^2. \tag{5}$$

Because the fourth-order terms are written as

$$F^{(4)} = \frac{\beta_1}{2}(\vec{\eta}'\cdot\vec{\eta}' + \vec{\eta}''\cdot\vec{\eta}'')^2 + \frac{\beta_2}{2}[(\vec{\eta}'\cdot\vec{\eta}' - \vec{\eta}''\cdot\vec{\eta}'')^2 + 4(\vec{\eta}'\cdot\vec{\eta}'')^2] \tag{6}$$

for $\beta_1, \beta_2 > 0$, we can find a minimum when $|\vec{\eta}'| = |\vec{\eta}''|$ and $\vec{\eta}' \perp \vec{\eta}''$. Notably, the weak coupling estimate [46] leads to $\beta_1/\beta_2 = -2$. Thus, we have to resort to the strong coupling effects in the following arguments in order to stabilize an A_1 phase.

It is convenient to introduce

$$\eta_\pm = \frac{1}{\sqrt{2}}(\eta_y \pm i\eta_z) \tag{7}$$

for $\mathbf{M} = (M_x, 0, 0)$ where we denote the x axis as the magnetic easy axis in this section. From Eq. (3) the quadratic term $F^{(2)}$ is rewritten in terms of $\eta_\pm$ and η_x as

$$F^{(2)} = \alpha_0\{(T - T_{c1})|\eta_+|^2 + (T - T_{c2})|\eta_-|^2 + (T - T_{c3})|\eta_x|^2\} \tag{8}$$

with

$$T_{c1,2} = T_{c0} \pm \frac{\kappa}{\alpha_0}M_x, \qquad T_{c3} = T_{c0} - \frac{b}{\alpha_0}M_x^2. \tag{9}$$

We have neglected the term $cM^2\vec{\eta}\cdot\vec{\eta}^\star$ in Eq. (3) because it causes the parallel shifts for T_{cj} $(j = 1, 2, 3)$ by the same amount. The actual second transition temperature is modified to

$$T'_{c2} = T_{c0} - \frac{\kappa M_x}{\alpha_0}\frac{\beta_1 - \beta_2}{2\beta_2} \tag{10}$$

because of the fourth-order GL terms in Eq. (5). Also, T_{c3} starts decreasing in the linear $|M_x|$ instead of M_x^2 mentioned above just near $|M_x| \ll 1$. This comes from the renormalization of T_{c3} in the presence of $|\eta_+|^2 \propto (T_{c1} - T)$ and $|\eta_-|^2 \propto (T_{c2} - T)$. Those terms give rise to the $|M_x|$-linear suppression of T_{c3} through fourth-order terms. Here we note that among the GL fourth-order terms, $\mathrm{Re}(\eta_x^2\eta_+\eta_-)$ in Eq. (5) becomes important in interpreting the H_{c2} data later because it is independent of the signs of the GL parameters β_1 and β_2. For

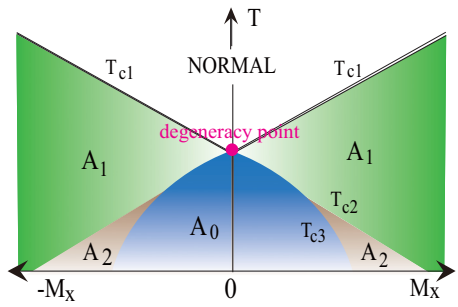

FIG. 1. Generic phase diagram in the T and M_x planes. T_{c1} (T_{c2}) for the A_1 (A_2) phase increases (decreases) linearly in M_x. The third phase A_0 decreases quadratically in M_x away from the degenerate point at $M_x = 0$.

$1 \leqslant \beta_1/\beta_2 \leqslant 3$,

$$T'_{c2} > T_{c2} = T_{c0} - \frac{\kappa}{\alpha_0} M_x. \tag{11}$$

This could lead to the modification of the otherwise symmetric phase diagram:

$$T_{c1} - T_{c0} = T_{c0} - T_{c2}. \tag{12}$$

The fourth-order contribution of Eq. (10) to T_{c2} may become important to quantitatively reproduce the H-T phase diagram, such as the asymmetric L-shape H_{c2} for $H \parallel b$ axis observed in UTe_2 [12].

Note that the ratio of the specific heat jumps to

$$\frac{\Delta C(T_{c1})}{\Delta C(T_{c2})} = \frac{T_{c1}}{T_{c2}} \frac{\beta_1}{\beta_1 + \beta_2}. \tag{13}$$

The jump at T_{c2} can be quite small for $T_{c1} \gg T_{c2}$. The FM moment M_x acts to shift the original transition temperature T_{c0} and split it into T_{c1}, T_{c2}, and T_{c3} as shown in Fig. 1. Here, the A_1 and A_2 phases correspond to $|\uparrow\uparrow\rangle$ pair and $|\downarrow\downarrow\rangle$ pair, respectively and the A_0 phase is $|\uparrow\downarrow\rangle + |\downarrow\uparrow\rangle$ for the spin quantization axis parallel to the magnetization direction M_x. According to Eq. (9), T_{c1} (T_{c2}) increases (decreases) linearly as a function of M_x while T_{c3} decreases quadratically as M_x^2 far away from the degeneracy point shown there (the red dot). The three transition lines meet at $M_x = 0$ where the three components η_i ($i = +, -, x$) are all degenerate, restoring SO(3) spin-space symmetry. Thus, away from the degenerate point at $M_x = 0$, the A_0 phase starting at T_{c3} quickly disappears from the phase diagram. Below T_{c2} (T_{c3}) the two components η_+ and η_- coexist, symbolically denoted by $A_1 + A_2$.

Note that because their transition temperatures are different, $A_1 + A_2$ is not the so-called A phase which is unitary, but generically nonunitary except at the degenerate point $M_x = 0$ where the totally symmetric phase is realized with time-reversal symmetry preserved. Likewise below T_{c3} all the components coexist: $A_1 + A_2 + A_0$ realizes.

Under an applied field with the vector potential $\mathbf{A}$, the gradient GL energy is given by

$$F_{\rm grad} = \sum_{\nu=x,y,z} \{K_x |D_x \eta_\nu|^2 + K_y |D_y \eta_\nu|^2 + K_z |D_z \eta_\nu|^2\}, \tag{14}$$

where $D_j = -i\hbar\partial_j - 2eA_j/c$ and the mass terms are characterized by the coefficients K_j ($j = x, y, z$) in D_{2h}. We emphasize here as seen from this form of Eq. (14) that H_{c2} for the three components each starting at T_{cj} ($j = 1, 2, 3$) intersects each other, never avoiding or leading to a level repulsion. The level repulsion may occur for the pairing states belonging to multidimensional representations (see, for example, [57–60] in UPt_3). The external field H implicitly comes into T_{cj} ($j = 1, 2, 3$) through $M_a(H)$ in addition to the vector potential A. This gives rise to the orbital depairing mentioned above.

B. Quasiparticle spectrum for general triplet state

If we choose $\vec{\eta}' = \eta_y \hat{y}$ and $\vec{\eta}'' = \eta_z \hat{z}$ with $\eta_x = 0$ for the magnetic easy x axis, the quasiparticle spectra are calculated by

$$E_{k,\sigma} = \sqrt{\epsilon(k)^2 + (|\vec{\eta}|^2 \pm |\vec{\eta} \times \vec{\eta}^\star|)\phi(k)^2} \tag{15}$$

or

$$E_{k,\sigma} = \sqrt{\epsilon(k)^2 + \Delta_\sigma(k)^2}, \tag{16}$$

where the gap functions for two branches are

$$\begin{aligned} \Delta_\uparrow(k) &= |\eta_y + \eta_z|\phi(k), \\ \Delta_\downarrow(k) &= |\eta_y - \eta_z|\phi(k), \\ \Delta_0(k) &= |\eta_x|\phi(k). \end{aligned} \tag{17}$$

Note that if $|\eta_z| = 0$, $\Delta_\uparrow(k) = \Delta_\downarrow(k)$, which is nothing but the A phase [43]. When $|\eta_y| = |\eta_z|$, $\Delta_\uparrow(k) \neq 0$ and $\Delta_\downarrow(k) = 0$, which is the nonunitary A_1 phase for $\eta_x = 0$. The gap in one of the two branches vanishes and the other remains ungapped. Therefore, if we assume that in the normal state $N_\uparrow(0) = N_\downarrow(0)$, the A_1 phase is characterized by having the ungapped DOS $N_\downarrow(0) = N(0)/2$ with $N(0) = N_\uparrow(0) + N_\downarrow(0)$. Generically, however, since $N_\uparrow(0) \neq N_\downarrow(0)$, that is, $N_\uparrow(0) > N_\downarrow(0)$ in the A_1 phase, which is energetically advantageous than the A_2 phase, the "residual DOS" is equal to $N_\downarrow(0)$, which is likely less–than–half rather than more–than–half physically. In the nonunitary state with the complex $\mathbf{d}$ vector, the time-reversal symmetry is broken.

In the most general case where all components η_x, η_y, and η_z are nonvanishing, the quasiparticle spectra are calculated by diagonalizing the 4×4 eigenvalue matrix. Namely, in terms of Eq. (17) the spectrum is given by

$$\begin{aligned} E_k^2 = \epsilon(k)^2 + \tfrac{1}{2}\big\{&\Delta_\uparrow^2(k) + \Delta_\downarrow^2(k) + 2\Delta_0^2(k) \\ &\pm \sqrt{[\Delta_\uparrow^2(k) - \Delta_\downarrow^2(k)]^2 + 4\Delta_0^2(k)[\Delta_\uparrow^2(k) + \Delta_\downarrow^2(k)]}\big\}. \end{aligned} \tag{18}$$

It is easy to see that this spectrum is reduced to Eq. (16) when $\Delta_0(k) = 0$. This spectrum characterizes the phase $A_1 + A_2 + A_0$ realized in UTe_2 under pressure as we will see shortly.

III. PROTOTYPES OF PHASE TRANSITIONS

Let us explain the phase diagram displayed in Fig. 2(a) by considering the action of the external field H_b applied to the magnetic hard b axis on the FM moment M_a, pointing parallel to the a axis. The a-axis component of the moment $M_a(H_b)$ generally decreases as it rotates toward the b axis as shown in Fig. 2(b). As discussed in the next section in more details

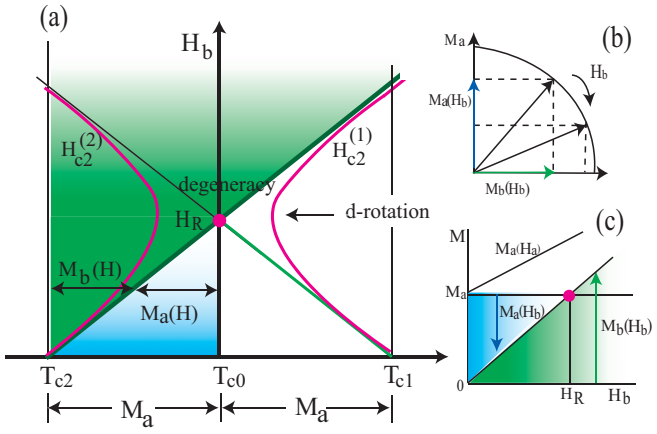

FIG. 2. (a) Prototype phase diagram in the T and H_b planes where H_b is parallel to the magnetic hard b axis and the moment M_a points to the easy a axis. The two transition lines of T_{c1} and T_{c2} (red curves) are separated by $2M_a$ at $H_b = 0$. Initially, T_{c1} decreases and T_{c2} increases as H_b increases toward the degeneracy point at T_R. There the projection of the FM moment M_a vanishes. Up to this field the SOC is assumed to lock the **d** vector, thus, T_{c1} and T_{c2} follow $M_a(H_b)$. Approximately above H_R by rotating the **d**-vector direction to follow the magnetization $M_b(H_b)$ (the green lines) instead of $M_a(H_b)$, $H_{c2}^{(1)}$ and $H_{c2}^{(2)}$ turn around their directions. (b) Under the perpendicular field H_b the spontaneous moment M_a rotates toward the b direction. The projection $M_b(H_b)$ of M_a on the b axis increases. (c) The rotation field H_R is indicated as the red dot where $M_b(H_b) = M_a(H = 0)$.

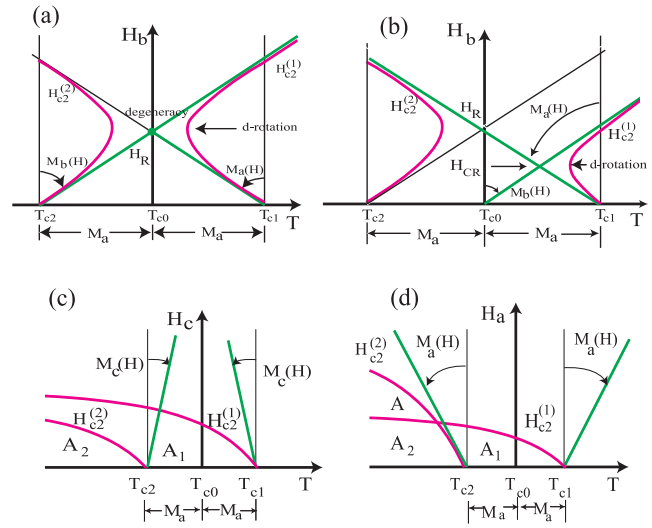

FIG. 3. Two types (a) and (b) of the phase diagram for $H \parallel b$ with the b axis (hard axis). (a) The same as in Fig. 2(a). (b) At H_{CR} defined by $M_b(H_b) = M_a(H_b)$, $H_{c2}^{(1)}$ turns around by rotating the **d** vector to follow M_b starting from T_{c0}. (c) $H \parallel c$ with the c axis (another hard axis). (d) $H \parallel a$ with the a axis (easy axis). The green lines are the respective magnetization curves and the red curves are $H_{c2}^{(1)}$ and $H_{c2}^{(2)}$.

based on experimental data, it is observed in URhGe through the neutron experiment [39]. Here we display the generic and typical magnetization curves of M_a and M_b in Fig. 2(c) where H_R denotes a characteristic field for $M_b(H_b) = M_a(H_b = 0)$. The induced moment M_b reaches the spontaneous FM moment M_a at zero field by rotating the FM moment, implying that the FM moment points to the b axis above H_R. Experimentally, it is realized by the so-called metamagnetic transition via a first-order transition in URhGe [39] and UTe_2 [14] or gradual change in UCoGe [61].

As displayed in Fig. 2(a), by increasing H_b, T_{c1} (T_{c2}) decreases (increases) according to Eq. (9). The corresponding $H_{c2}^{(1)}$ and $H_{c2}^{(2)}$ are starting there, whose forms will be derived shortly. The two transition lines $T_{c1}(H_b) = T_{c2}(H_b)$ meet at $H_b = H_R$. As H_b is further increased, T_{c1} also increases by rotating the **d**-vector direction such that the **d** vector becomes perpendicular to $\mathbf{M}_b$, which maximally gains the magnetic coupling energy $i\kappa\vec{M}\cdot\vec{\eta}\times\vec{\eta}^{\star}$ in Eq. (3). This process occurs gradually or suddenly, depending on the situations of the magnetic subsystem and the spin-orbit coupling that locks the **d** vector to the underlying lattices. Therefore, H_R may indicate simultaneously the **d**-vector rotation. It should be noted, however, that if the spin-orbit coupling is strong, the **d**-vector rotation is prevented. In this case H_{c2}^{b} exhibits a Pauli limited behavior as observed in UTe_2 under pressure [28].

In Fig. 3 we show prototype phase diagrams for different situations. In addition to that displayed in Fig. 3(a), which is the same as in Fig. 2(a), there is the case in which T_{c1} is bent before reaching H_R as shown in Fig. 3(b). The magnetization curve $M_b(H_b)$ starting at T_{c0} exceeds the decreasing M_a at a lower field H_{CR} defined by $M_b(H_b) = M_a(H_b)$. $H_{c2}^{(1)}$ turns around there by rotating the **d** vector. We will see this case in the following analysis.

In the H_c case for the field direction parallel to another hard c axis, the phase diagram is shown in Fig. 3(c). Since H_c does not much influence on $M_a(H_c)$, both $H_{c2}^{(1)}$ and $H_{c2}^{(2)}$ are suppressed by the orbital depression of H_c. When the magnetic field is applied to the magnetic easy a axis, the spontaneous moment $M_a(H_a)$ increases monotonically, as shown in Fig. 3(d). According to Eq. (9), T_{c1} (T_{c2}) increases (decreases) as H_a increases. Thus, theoretically $H_{c2}^{(1)}$ can have a positive slope at T_{c1}. However, the existing data on UCoGe [62] indicate that it is negative, as seen shortly. This is because the strong orbital depairing $H_{c2}^{\prime 0}$ overcomes the positive rise of T_{c1}. Moreover, $H_{c2}^{(2)}$ is strongly suppressed by both T_{c2} and the orbital effect $H_{c2}^{\prime 0}$, resulting in a low H_{c2}^{a}, compared with H_{c2}^{b}. This H_{c2} anisotropy is common in these compounds [5]. From the above considerations, the enhanced H_{c2}^{b} is observed because the higher part of the field in H_{c2} belongs to $H_{c2}^{(2)}$, which has a positive slope.

Within the GL scheme it is easy to estimate H_{c2} as follows. We start with the H_{c2} expression valid near the upper critical temperature and low field, which can be derived by combing Eqs. (8) and (14) and minimizing the free energy,

$$H_{c2}(T) = A^{(0)}\{T_c(H_{c2}) - T\} \tag{19}$$

with $A^{(0)} = \frac{\Phi_0}{2\pi\hbar^2}4m\alpha_0$, m effective mass, and Φ_0 quantum unit flux. T_c depends on H though $M_a(H)$ is as described above. We assume this simple H_{c2} formula to estimate the phase diagram at lower temperatures instead of that given by the standard Werthamer-Helfand.Hohenberg (WHH) formula [63], which describes the behavior at low temperatures beyond the above GL formula more accurately. We denote it as H_{c2}^{WHH}.

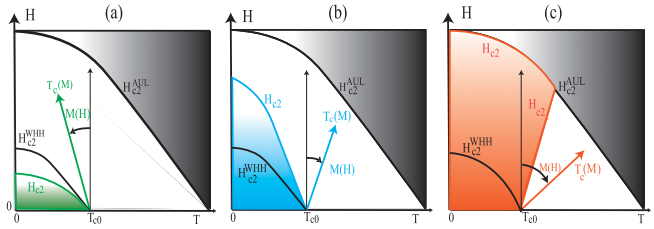

FIG. 4. H_{c2} changes due to the competition between the orbital depairing and $T_c(M)$. (a) $T_c(M)$ decreases as a function of the applied field H. The orbital depairing is added up to further depress H_{c2} than $H_{c2}^{\rm WHH}$. (b) $T_c(M)$ increases as a function of the applied field H, competing with the orbital depairing. The resulting H_{c2} is enhanced compared with $H_{c2}^{\rm WHH}$. (c) $T_c(M)$ increases strongly as a function of the applied field H. H_{c2} has a positive initial slope and keeps growing until hitting the absolute upper limit $H_{c2}^{\rm AUL}$. Then, H_{c2} follows this boundary.

The initial slope of H'_{c2} at T_c is simply given by

$$H'_{c2}(T) = A^{(0)}\frac{dT_c}{dH_{c2}}H'_{c2} - A^{(0)}. \tag{20}$$

It is seen that if $dT_c/dH = 0$ for the ordinary superconductors, $H_{c2}^{\prime 0}(T) = -A^{(0)} < 0$. The slope $H'_{c2}(T)$ is always negative. However, Eq. (20) is expressed as

$$H'_{c2}(T) = \frac{-A^{(0)}}{1 - A^{(0)}\left(\frac{dT_c}{dH_{c2}}\right)} \tag{21}$$

or

$$\frac{1}{|H'_{c2}|} = \frac{1}{|H_{c2}^{\prime 0}|} + \left|\frac{dT_c}{dH_{c2}}\right| = \frac{1}{|H_{c2}^{\prime 0}|} + \frac{1}{\left|\frac{dH_{c2}}{dT_c(H)}\right|}. \tag{22}$$

The condition for attaining the positive slope $H'_{c2}(T) > 0$ implies $|H_{c2}^{\prime 0}| > (\frac{dH}{dT_c})$ at H_{c2}. This is a necessary condition to achieve S-shaped or L-shaped H_{c2} curves experimentally observed. This is fulfilled when $|H_{c2}^{\prime 0}|$ is large enough, that is, the orbital depairing is small, $|\frac{dT_c}{dH}|$ at H_{c2} is large, or the T_c rise is strong enough.

It is noted that when $1 - A^{(0)}(\frac{dT_c}{dH_{c2}}) = 0$, the $H_{c2}(T)$ curve has a divergent part in its slope, which is observed in UCoGe as a part of the S shape. It is clear from the above that when $dT_c/dH < 0$, $|H'_{c2}(T)| < |H_{c2}^{\prime 0}|$ because the two terms in Eq. (22) are added up to further depress $H_{c2}(T)$. In this case the slope $|H'_{c2}|$ is always smaller than the original $|H_{c2}^{\prime 0}|$ as expected.

In Fig. 4 we show the changes of H_{c2} when the competition between the orbital suppression and $T_c(M)$ varies. We start from the orbital-limited $H_{c2}^{\rm WHH}$ curve with T_c unchanged as a standard one. When $T_c(M)$ decreases with increasing H, the resulting H_{c2} is further suppressed compared with $H_{c2}^{\rm WHH}$ as shown in Fig. 4(a). $T_c(M)$ as a function of H through $M(H)$ becomes increasing as shown in Fig. 4(b), H_{c2} is enhanced compared to $H_{c2}^{\rm WHH}$, exceeding the $H_{c2}^{\rm WHH}$ value. Figure 4(c) displays the case where $T_c(M)$ increases stronger than that in Fig. 4(b), H_{c2} has a positive slope and keeps increasing until it hits the upper limit $H_{c2}^{\rm AUL}$. There exists the absolute upper limit (AUL) for H_{c2}. Even though $T_c(M)$ keeps increasing with increasing $M(H)$, H_{c2} terminates at a certain field because a material has its own coherent length ξ which absolutely limits $H_{c2}^{\rm AUL} = \Phi_0/2\pi\xi^2$. Beyond $H_{c2}^{\rm AUL}$ there exists no superconducting state. The precise temperature dependence of $H_{c2}^{\rm AUL}$ is unknown and should be investigated in near future by a microscopic theory.

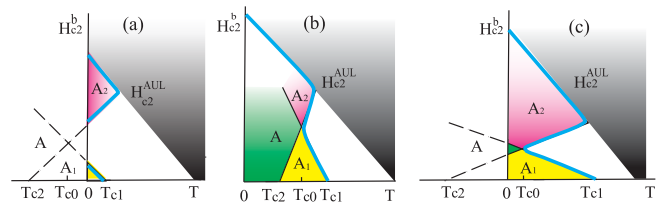

FIG. 5. Schematic typical phase diagrams for H parallel to the b axis with A_1, A_2, and A phases, whose structure depends on the position of T_{c0} and the separation of T_{c1} and T_{c2}. The A phase is a mixture of A_1 and A_2 phases. The absolute upper limit $H_{c2}^{\rm AUL}$ is indicated as the gray region. (a) The reentrant SC situated at high fields such as in URhGe. (b) S-shape H_{c2} with the double transitions from the A_1 to the A phase such as in UCoGe. (c) L-shape H_{c2} where the high field phase is the A_2 phase such as in UTe_2.

There could be several types of H_{c2}^b curves for H applied to the b axis (hard axis), depending on several factors: (i) the magnitude of the spontaneous moment M_a, (ii) its growth rate against H_b, (iii) the coupling constant κ, and (iv) the relative position of T_{c0} on the temperature axis.

Possible representative H_{c2}^b curves are displayed in Figs. 5(a)–5(c). When the hypothetical T_{c0} is situated in the negative temperature side, the realized phase is only the A_1 phase at $H_b = 0$. In high field regions SC reappears as the reentrant SC (RSC) by increasing $M_b(H_b)$, which is shown in Fig. 5(a). The reentrant SC is separated from the lower SC.

As shown in Fig. 5(b) the two transition temperatures T_{c1} and T_{c2} are realized at $H_b = 0$, that is, it shows double transitions at zero field, giving rise to the A_1 and A_2 phases. The three phases A_1, A_2, and A appear in a finite-H_b region where the A phase is a mixture of A_1 and A_2 phases. H_{c2} could have an S shape. This corresponds to either Fig. 3(a) or 3(b).

When the separation between T_{c1} and T_{c2} becomes wider because of increasing the spontaneous moment M_a and/or the larger magnetic coupling κ, H_{c2} has an L shape as displayed in Fig. 5(c). This could happen also when the moment rotation field T_R is situated at relatively lower field than the overall H_{c2}.

In the following we discuss those typical H_{c2} behaviors based on the realistic magnetization curves for each compound, reproduce the observed H_{c2} curves, and predict the existence of the multiple phase diagram. Note that the resulting H_{c2} curves do not sensitively depend on the choice of the triplet pairing function.

IV. MAGNETIZATION CURVES

In order to understand their peculiar H_{c2} shapes and resulting pairing symmetry in three compounds, it is essential to know their magnetic responses to applied magnetic fields. Here we analyze their magnetism and estimate the magnetization curves of the spontaneous moment under the transverse

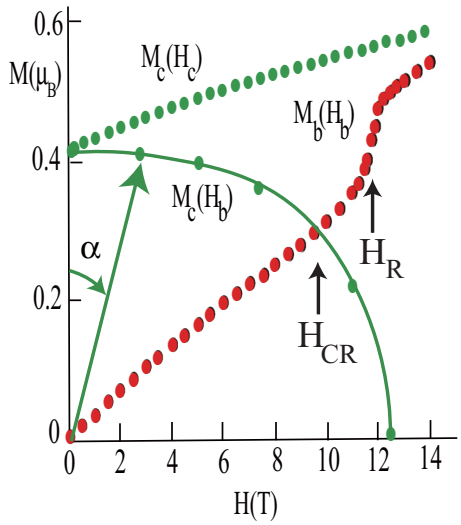

FIG. 6. The ferromagnetic spontaneous moment $M_c(H_b)$ rotation indicated by the green arrow under the field $H \parallel b$ in URhGe. At $H_b = H_R$, it completely orients along the b-axis direction via a first-order transition where $M_b(H_b)$ shows a jump of the magnetization. H_{CR} is defined by the field $M_c(H_b) = M_b(H_b)$. The rotation angle α from the c axis is measured by neutron experiment [39]. The magnetization curves $M_b(H_b)$ and $M_c(H_c)$ are from [64].

field, which is not probed by conventional magnetization measurements. In the following, we consider the cases of URhGe and UCoGe, and UTe_2 with the c axis and a axis are the easy axes, respectively, as tabulated in Table I. We mainly discuss URhGe as a typical example. The concepts introduced here are applied to the other systems with appropriately changing the notation for the magnetic easy axis.

A. Rigid rotation picture: Spontaneous moment rotation

When the applied field H_b is directed to the hard axis, or the b axis, the spontaneous moment $M_c(H_b)$ pointing to the c axis in URhGe rotates gradually toward the applied field direction. At around $H_R = 12$ T, $M_c(H_b)$ quickly turns to the b direction by rotating the moment as shown in Fig. 6. We define the crossing field H_{CR} at which $M_c(H_b) = M_b(H_b)$. Note that H_R and H_{CR} are different concepts as is clear from Fig. 6 and also in UCoGe where $H_{CR} \sim$ a few T and $H_R =$ 45 T [61]. Simultaneously and correspondingly, the $M_b(H_b)$ moment jumps via a first-order transition. Above $H_b > H_R$ the spontaneous moment is completely aligned along the b axis as seen from Fig. 6. This phenomenon is often called as the metamagnetic transition. But this is just the moment rotation since it is demonstrated that the total magnetization $\sqrt{M_c^2(H_b) + M_b^2(H_b)}$ hardly changes and remains a constant during this first-order transition process [39].

This implies that $M_c(H_b) = M_c \cos[\alpha(H_b)]$, and $M_b(H_b) = M_c \sin[\alpha(H_b)]$ with $\alpha(H_b)$ being the rotation angle of $M_c(H_b)$ from the c axis. The rotation angle $\alpha(H_b)$ is accurately measured by the neutron scattering experiment by Lévy *et al.* [39] who construct the detailed map of the rotation angle in the H_b and H_c planes. This rotation process is mirrored by the magnetization curve of $M_b(H_b)$ so that the projection of $M_c(H_b)$ onto the b axis manifests itself on $M_b(H_b)$ as shown in Fig. 6.

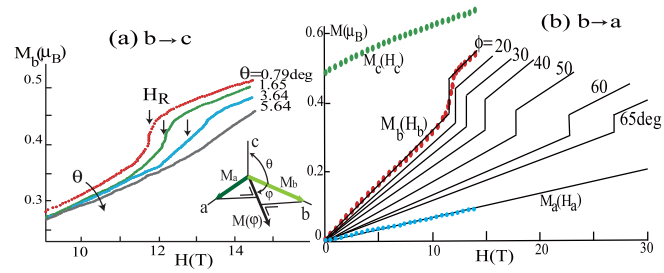

FIG. 7. (a) The magnetization component of $M_b(H)$ in URhGe under the field direction tilted from the b axis toward the c axis by θ, estimated from the experimental data of $M(H)$ [69]. The inset shows the coordinates and the projections of M_a and M_b onto the ϕ axis. (b) The magnetization $M(H)$ in URhGe under the field direction tilted from the b axis toward the a axis by ϕ estimated from the experimental data (dots) of $M(H)$ [64], including magnetization curves for three a, b, and c directions for reference.

The crossing of $M_b(H_b)$ and $M_c(H_b)$ occurs around at $H_{CR} = 9 \sim 10$ T, corresponding to roughly $M_c(H_b)/\sqrt{2} \sim M_b(H_b)$. That is, $M_c(H_b)$ rotates by the angle $\alpha = 45^\circ$ from the c axis at H_{CR}. However, since the moment rotation process depends on materials, H_{CR} is only estimated within an order of magnitude. This first-order phase transition phenomenon in URhGe under the transverse field is neatly described by Mineev [65] using the GL theory. This is within a more general framework of the so-called metamagnetic transition theory based on the GL phenomenology [66–68] for itinerant ferromagnets.

Those considerations based on the experimental facts demonstrate to hold "a rigid moment rotation picture." We assume this picture applicable to the other compounds too.

B. Extraction of the M_b moment for the tilted fields from the b-axis data

When the applied field direction is rotated from the b axis toward the easy axis c by the angle θ, the magnetization curves are measured by Nakamura *et al.* [69]. It is obvious that the measured magnetization $M(\theta)$ contains the contribution from the spontaneous moment $\mathbf{M}_c$ projected onto the applied field direction, that is, $M_c \sin(\theta)$. This is confirmed experimentally at least at lower fields up to $H < 5$ T and $T = 2$ K [70]. Thus in this situation, we can extract the $M_b(H)$ curves by simply subtracting the contribution $M_c \sin(\theta)$ from the measured data [69]. The result is shown in Fig. 7(a). It is seen that by increasing the angle θ, the first-order transition field H_R shifts to higher fields and the jump gets smaller compared to the b-axis case, reflecting that the moment projection onto the applied field direction decreases. This method is valid only for the small angle θ and relatively small field regions because here the M_c moment is assumed to be fixed under the action of small field component along the c axis.

It may be difficult to extract reliably the $M_b(H)$ information for further high fields even though the tilting angle is small, and also for larger angles θ. There are two factors to be taken into account, which are internally related: One is that the c-component magnetic field acts to prevent the moment from further rotating it toward the b axis upon increasing tilting field H by θ from the b axis. This "rotation angle locking

effect" becomes important for the field just before $H_R(\theta)$ where the moment ultimately rotates completely along the b axis in the higher fields. The other factor to be considered is the modification of the free-energy landscape of the M_b versus M_c space.

The first-order transition of the moment rotation is described by Mineev [65] who considers the competition between the ferromagnetic state at M_c and the paramagnetic state with M_b stabilized by the Zeeman effect due to the external field H_b within a GL free-energy theory. The transverse field H_b necessarily destabilizes the second-order FM phase transition at H_R because H_b contributes negatively to the quartic term coefficient of M_c^4, giving rise to a first-order transition. The extra term coming from the tilting field helps to stabilize the ferromagnetic state, preventing the first-order transition, thus making H_R to higher field and the magnetization jump smaller. Thus, it is not easy to extract reliably the $M_b(H)$ under this free-energy landscape modification. In the following, we confine our arguments for small θ and use approximate $M_b(H)$ forms, which are enough for our purposes to understand the peculiar H_{c2}.

C. Applied field rotation from the *b* axis to the hard axis

In the case for the tilting angle ϕ from the b axis toward the other hard axis a of URhGe, it is known [71] that $H_R(\phi)$ is scaled to $H_R(\phi) \propto 1/\cos(\phi)$, which is also the case in UTe_2 [15]. This means that only the M_b projection onto the field direction matters to understand the magnetization process. Therefore, we can easily reconstruct the $M(\phi)$ by using the experimental data of $M_b(H_b)$ except for the fact that the induced $M_a(\phi)$ also contributes to $M(\phi)$. This can be accomplished by an "elliptic formula" derived as follows:

We start with $M_b(H_b)$ and $M_a(H_a)$ measured by usual magnetization experiments shown in Fig. 7(b). Assuming the linearity assumption $M_b(\phi) = \chi_b H\cos(\phi)$ and $M_a(\phi) = \chi_a H\sin(\phi)$ with χ_i $(i = a, b)$ being the magnetic susceptibility, we add up the two components as explained in the inset of Fig. 7(a):

$$\begin{aligned} M(\phi) &= M_b\cos\phi + M_a\sin\phi \\ &= [\chi_b\cos^2(\phi) + \chi_a\sin^2(\phi)]H \\ &= M_b(H_b)\cos^2\phi + M_a(H_a)\sin^2\phi. \end{aligned} \tag{23}$$

We call it an "elliptic formula." Since the rotation field is given by

$$H_R(\phi) = \frac{H_R^b}{\cos(\phi)} \tag{24}$$

with H_R^b the rotation field for the b axis, we obtain at $H = H_R$

$$M(\phi) = M_b(H_R)\left(\cos\phi + \frac{\chi_a}{\chi_b}\frac{\sin^2\phi}{\cos^2\phi}\right). \tag{25}$$

This formula gives the magnetization curve consisting of a straight line from $H = 0$ up to H_R. The magnetization jump at H_R is calculated by projecting the jump δM_b in $M_b(H_b)$, namely, $\delta M_b\cos(\phi)$.

The resulting reconstructions of $M(\phi)$ for various tilting angles are shown in Fig. 7(b). By construction, when $\phi \to 90^\circ$, $M(\phi) \to M_a(H_a)$. We notice that the resulting $M(\phi)$ includes the contribution from M_a. Those results should be checked experimentally and will be used to reproduce the RSC in URhGe. As shown in Fig. 8(b) this idea is also applied to UTe_2 where the RSC appears centered around $\theta = 35^\circ$ from the b axis toward another hard axis c.

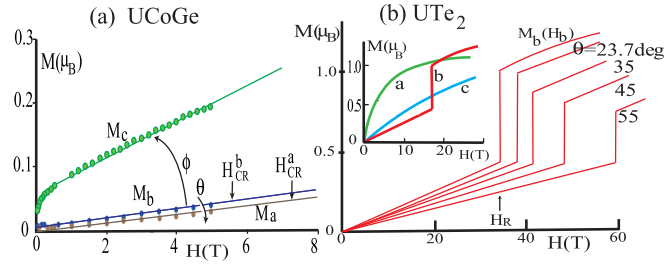

FIG. 8. (a) The magnetization curves for three a, b, and c axes in UCoGe. Here the crossing points H_{CR}^b and H_{CR}^a at which each curve surpasses the spontaneous moment $M_c(H = 0) = 0.06\mu_B$. (b) The magnetization curves of $M_b(H)$ for the field directions tilted from the b axis toward the c axis by the angle θ (degrees) in UTe_2. $\theta = 23.7^\circ$ corresponds to $H \parallel (011)$ direction measured by [72]. Those are estimated by the method explained in the main text. The inset shows the magnetization curves for three a, b, and c axes in UTe_2. H_R is the first-order transition for the moment rotation from the a axis to the b axis.

As a final comment on the magnetization of UCoGe shown in Fig. 8(a), it should be mentioned that since $H_R \sim 45$ T [61], for the following discussions on this system the characteristic magnetic fields $H_{CR}^b \sim 6$ T and $H_{CR}^a \sim 7$ T are relevant to notice from this figure. We also note that two magnetization curves M_b and M_a behave similarly. It is anticipated that H_{c2} for the two directions should be resemble. This is indeed the case as will be seen next.

V. APPLICATION TO EXPERIMENTS ON THREE COMPOUNDS

Let us now examine the present theory to understand a variety of experiments on the three compounds URhGe, UCoGe, and UTe_2. In order to clarify the essential points of the problem and for the discussions followed to be transparent, and to minimize the free adjustable parameters, we take a simplified minimal version of the present theory. It is quite easy to finely tune our theory by introducing additional parameters such as β_1 and β_2 in the GL theory (3) for each compound if necessary. We assume that

$$\begin{aligned} T_{c1} &= T_{c0} + \kappa M_a, \\ T_{c2} &= T_{c0} - \kappa M_a, \\ T_{c3} &= T_{c0} - bM_a^2 \end{aligned} \tag{26}$$

for the spontaneous FM moment M_a with the easy a axis. We have redefined κ/α_0 as κ and b/α_0 as b, ignoring the correction in Eq. (10) from the higher-order GL terms. Since κ is a converter of the units from μ_B to K, we further simplify the notation in that κM having the dimension of temperature in K is denoted as M in K in the following phase diagrams. We use the κ values for three compounds throughout this paper

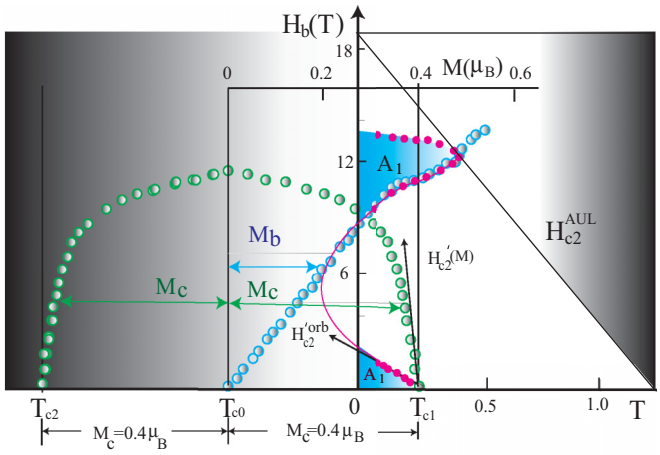

FIG. 9. The phase diagram for the $H_b(T)$ versus $T(K)$ plane. $M_c(H_b)$ is estimated from the neutron scattering data in Ref. [39] and $M_b(H_b)$ comes from the magnetization curve measured in Ref. [64]. The red dots for H_{c2} are the experimental data points in Ref. [5]. The red continuous line indicates H_{c2} which starts at T_{c1} and is suppressed by the orbital depairing effect. It reappears again by following the formula $T_{c1}(H_b) = T_{c0} + \kappa M_b(H_b)$ near $H_R = 11$ T. $H_{c2}^{\prime orb}$ and $H_{c2}'(M)$ are the slopes due to the orbital depairing and $T_{c1}(M_b)$, respectively.

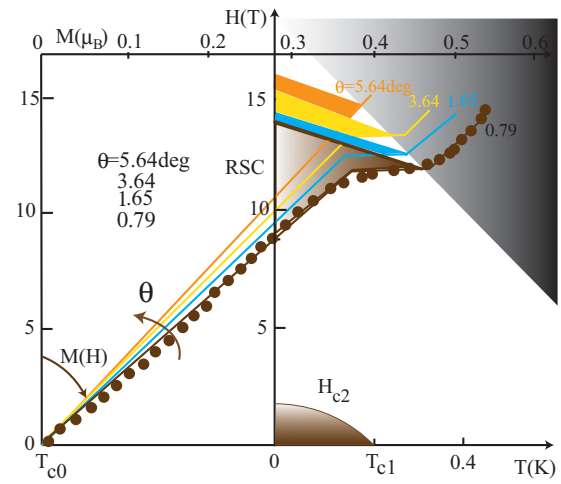

FIG. 10. Reentrant SC (Ref. [71]) for various θ values measured from the b axis ($\theta = 0$) toward the c axis in URhGe. As θ increases (0.79°, 1.65°, 3.64°, and 5.64°), the magnetization curves (far left scale) starting at T_{c0} grow slowly, pushing up the RSC regions to higher fields. The magnetization data are from Fig. 7(a) for $\theta \neq 0$ and Ref. [64] for $\theta = 0$.

as shown in Table I where the magnetic properties are also summarized.

In the following, we intend to produce the observed H_{c2} curves only qualitatively, not quantitatively. This is because the experimental H_{c2} shapes somewhat depend on the experimental methods. For example, see Fig. 1 in Ref. [73] where H_{c2} shapes slightly differ from each other, depending on the criteria adopted either by the midpoint of the resistivity drop, the zero resistivity, or by thermal conductivity. We here consider the sharpest curve among them when several choices are available.

A. $H \parallel b$: Reentrant SC

URhGe exhibits the ferromagnetic transition at $T_{\rm Curie} = 9.5$ K where the magnetic easy axis is the c axis and the FM moment $M_c = 0.4\mu_B$. The superconducting transition is at $T_c = 0.4$ K under the ferromagnetic state which is persisting to the lowest T. When the field H is applied parallel to the b axis, the superconducting state reappears in a higher field region while the low field SC phase disappears at $H_{c2} \sim 2$ T. This reentrant superconducting state (RSC) is explained in Fig. 9, using the knowledge shown in Fig. 7.

First we plot the magnetization curves for $M_c(H_b)$ and $M_b(H_b)$ in the H-T plane by choosing the $\kappa = 2.0$ K/μ_B in Eq. (26) with M_a replaced by M_c. $M_c(H_b)$ starts from T_{c1} and T_{c2} and decreases by increasing H_b which acts to rotate the spontaneous ferromagnetic moment toward the b axis. Thus, $T_{c1}(H_b) = T_{c0} + \kappa M_c(H_b)$ and $T_{c2}(H_b) = T_{c0} - \kappa M_c(H_b)$ decreases and increases, respectively, with increasing H_b according to Eq. (26). The splitting $2\kappa M_c(H_b)$ between $T_{c1}(H_b)$ and $T_{c2}(H_b)$ diminishes and meets at the rotation field $H_R = 12$ T where the two transition temperatures are going to be degenerate. $M_b(H_b)$ starting at T_{c0} quickly increases there. Thus, as shown in Fig. 9, H_{c2} starting at T_{c1} disappears at a low field because the orbital depairing dominates over the magnetization effect as explained above. Namely, since the decrease of $T_{c1}(H_b)$ is slow as a function of H_b, H_{c2} obeys the usual WHH curve, a situation similar to that shown in Fig. 4(a). Here $|H_{c2}'(M)| \gg |H_{c2}^{\prime orb}|$.

However, in the higher fields the upper transition temperature $T_{c1}(H_b)$ becomes

$$T_{c1}(H_b) = T_{c0} + \kappa M_b(H_b) \tag{27}$$

by rotating the **d** vector so that now it is perpendicular to the b axis to follow the magnetization $M_b(H_b)$. This **d**-vector rotation field corresponds to the field where

$$T_{c1}(H_b) = T_{c0} + \kappa M_c(H_b) \simeq T_{c0} + \kappa M_b(H_b), \tag{28}$$

namely, the $M_c(H_b)$ vector projection onto the b axis $M_c/\sqrt{2} \sim M_b(H_b)$ as understood from Fig. 6. Since $M_b(H_b)$ is strongly enhanced at and above H_R, the A_1 phase reappears by following the magnetization curve $T_{c0} + \kappa M_b(H_b)$. It ultimately hits the H_{c2}^{AUL} boundary. The RSC finally ceases to exist beyond this boundary. This corresponds to that in Fig. 4(c). The existence of the H_{c2}^{AUL} will be demonstrated later in Fig. 14 where we compile various H_{c2} data for URhGe, including those under hydrostatic pressure [74] and uniaxial pressure [75] along the b axis.

B. θ rotation from b to c axis

When the direction of the magnetic field turns from the b axis to the easy c axis, T_R moves up to higher fields and disappears quickly around $\theta \sim 5°$ as shown in Fig. 7(a). According to those magnetization behaviors, we construct the H_{c2} phase diagram in Fig. 10. It is seen that the field direction tilting away from the b axis to the c axis results in the decrease of the magnetization $M_b(H)$, corresponding to the counterclockwise changes of the magnetization curves in Fig. 10. Thus, the RSC

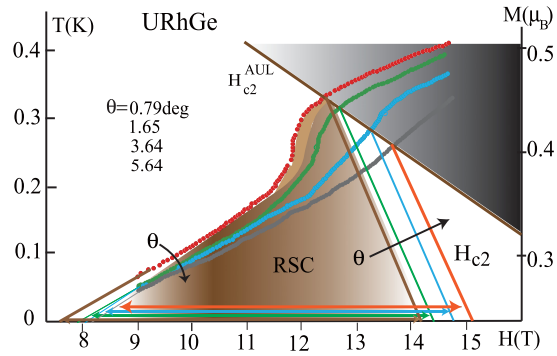

FIG. 11. Detailed RSC structures (Ref. [71]) in T-H plane (left scale) are displayed. The triangle areas in each θ are RSC. RSC moves right as θ increases. The magnetization curve data (right scale) corrected as explained in Fig. 7(a) are originally from Ref. [69].

region shifts to higher fields with shrinking their areas and eventually disappears by entering the H_{c2}^{AUL} region.

The detailed phase diagram in the reentrant region is depicted in Fig. 11 where the magnetization curves of $M_b(H)$ in Fig. 7(a) are overlaid. According to the present theory, H_{c2} follows faithfully $M_b(H)$ in the high fields because the strong increase tendency of the magnetization $M_b(H)$ overcomes the orbital depression. The characteristics of those phase diagrams are as follows. As θ increases, (1) the RSC moves up to further higher fields; (2) as H further increases, within the small angles of θ up to $6^\circ \sim 7^\circ$, the RSC fades out upon entering H_{c2}^{AUL} region.

Those characteristics (1) and (2) nicely match with the experimental observations. The trianglelike shapes for RSC will be seen later in UTe_2 (see Fig. 23).

C. ϕ rotation from b to a axis

When the magnetic field direction turns to the other hard a axis from the b axis by the angle ϕ, the expected magnetization curves are evaluated in Fig. 7(b). Using those magnetization curves, we construct the H_{c2} phase diagrams for various ϕ values in Fig. 12. As the angle ϕ increases, the

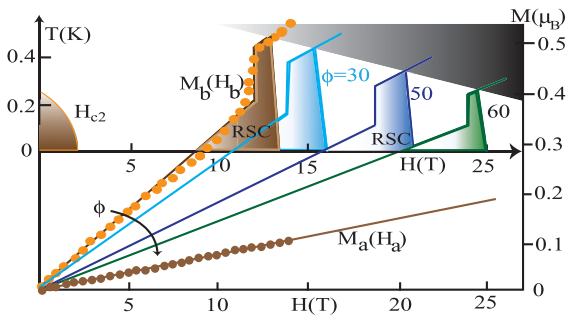

FIG. 12. RSC phase diagram in the T-H plane for various fields rotated from the b axis toward the a axis by the angle ϕ. This is constructed by using the magnetization data (right scale) shown in Fig. 7(b). When the magnetization hits the real axis $T > 0$, RSC appears in high field regions. The lower field H_{c2} is common for all ϕ.

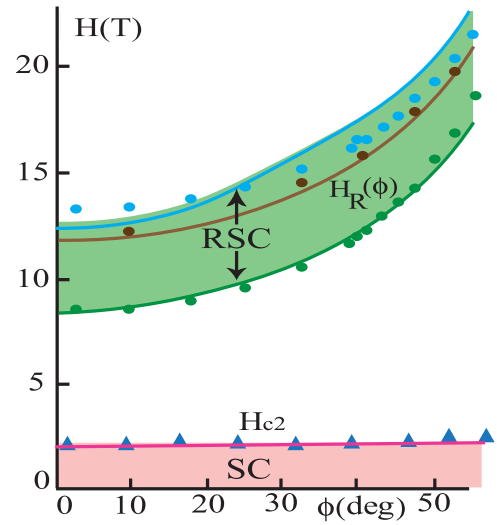

FIG. 13. Phase boundary of the reentrance SC (RSC) as a function of the angle ϕ measured from the b axis to the a axis constructed from Fig. 12. The blue (green) line indicates the upper (lower) boundary of the RSC. The brown line is the magnetization rotation field $H_R(\phi)$. The dots are experimental data points by Ref. [71]. The triangles denote the lower field H_{c2} which is almost independent of ϕ.

magnetization $M(H)$ decreases, corresponding to the clockwise changes in Fig. 12 and the first-order rotation field H_R is pushed to higher fields simply because of the projection effect onto the b axis as mentioned in Sec. IV C. As a consequence, the RSC moves to higher fields persisting up to higher angle ϕ until finally entering H_{c2}^{AUL} region. It is confirmed experimentally that it persists at least up to $H_{c2} \sim 25$ T [39]. According to the present results, the RSC can exist still to higher fields. This can be checked by experiments.

Here we notice an important fact that in order to explain the persistence of RSC as a function of ϕ up to higher fields, it is essential to use the magnetization curves in Fig. 7(b) where the magnetization contains the component M_a in addition to M_b. It is clear that only M_b fails to reproduce the RSC phase diagram. This means that the **d** vector rotates so as to follow both components M_a and M_b, thus, the **d** vector is always perpendicular to the vectorial sum $\mathbf{M}_a + \mathbf{M}_b$. This is contrasted with the θ rotation case where the **d** vector is perpendicular to $\mathbf{M}_b$. This intriguing anisotropy in the **d**-vector rotation relative to the magnetic easy axis might be related to the underlying magnetism in URhGe and/or the spin structure of the Cooper pair symmetry assumed as SO(3) originally. This spin-space anisotropy should be investigated in the future.

In Fig. 13 we summarize the phase boundary of the RSC determined above. The band of the RSC region is tightly associated with the $H_R(\phi)$ curves, which are proportional to $H_R(\phi) \propto 1/\cos(\phi)$. This is contrasted with the lower field H_{c2} which is nearly independent of the angle ϕ. The intrinsic H_{c2} anisotropy is quite small in URhGe. This means the importance of the magnetization rotation field $H_R(\phi)$, ensuring the appearance of the RSC, and pointing to the simple mechanism for the origin of RSC. It grossly follows the $\mathbf{M}_b$ projection onto the b axis. This is also true for the RSC in UTe_2, which will be explained shortly. The physics is common.

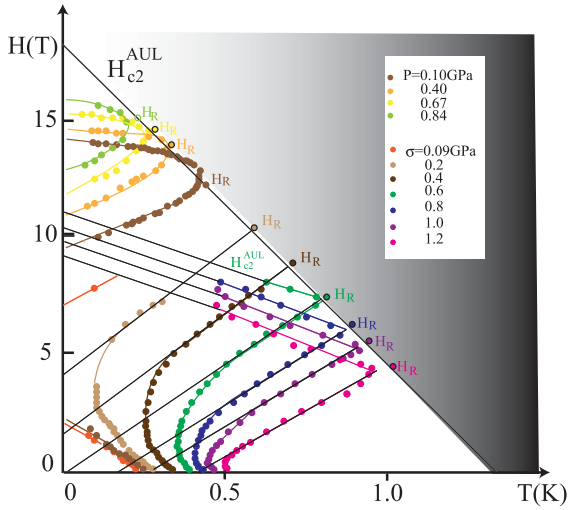

FIG. 14. Phase diagram for $H \parallel b$ taken under hydrostatic pressure (Ref. [74]) and uniaxial pressure along the b axis (Ref. [75]) on URhGe. All data at the rotation field H_R line up along the H_{c2}^{AUL} boundary, evidencing the existence of H_{c2}^{AUL}.

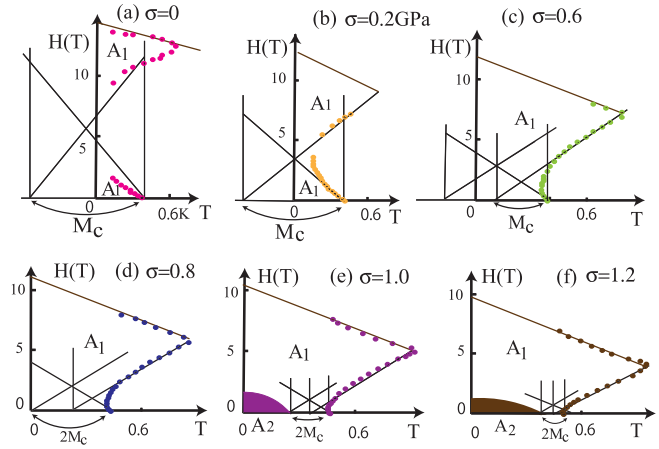

FIG. 16. Phase diagrams ($H \parallel b$) under uniaxial pressure, including the ambient pressure (a) in Fig. 9 and $\sigma = 1.0$ GPa (e) in Fig. 15. The data are from Ref. [75]. Continuous and systematic evolution of the multiple phase diagrams with guide lines are seen. (a) $\sigma = 0$ GPa, (b) $\sigma = 0.2$ GPa, (c) $\sigma = 0.6$ GPa, (d) $\sigma = 0.8$ GPa, (e) $\sigma = 1.0$ GPa, and (f) $\sigma = 1.2$ GPa.

D. Pressure effects

Before starting out to analyze the experimental data taken under hydrostatic [74] and uniaxial pressure [75] on URhGe, we summarize the relevant data for the H_{c2} phase diagram with the field applied to the b axis in Fig. 14. Here we list up the data under hydrostatic pressure and uniaxial pressure along the b axis. (1) It is clear to see that all the H_{c2} are limited by the common boundary H_{c2}^{AUL}. Beyond H_{c2}^{AUL} there exist no H_{c2} data. (2) It is also evident to see that the H_R data points under pressure remarkably line up along the bottom of the boundary, forming H_{c2}^{AUL} as an envelope. In the following we utilize those experimental facts and take into account those in investigating and reconstructing the H_{c2} phase diagrams.

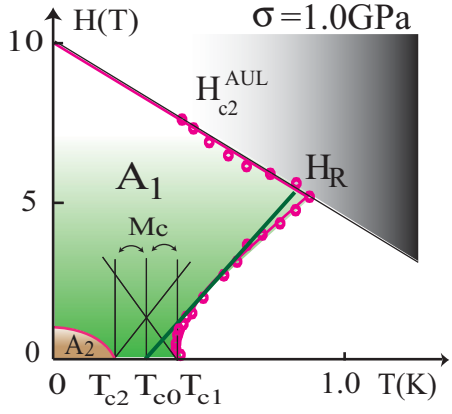

FIG. 15. Multiple phase diagram consisting of the A_1 and A_2 phases under uniaxial pressure $\sigma = 1.0$ GPa in URhGe. The data points of $H_{c2} \parallel b$ are taken from Ref. [75]. Two transitions at T_{c1} and T_{c2} separated by $2M_c$ are identified. H_R is the moment rotation field found experimentally [75]. The green line indicates the magnetization curve of M_b starting at T_{c0}.

In Fig. 15 we show the H_{c2} data points taken when H is applied along the b axis under uniaxial pressure $\sigma = 1.0$ GPa, which is listed in Fig. 14. Those data are explained in a similar way shown above. Here H_{c2} starting at T_{c1} is strongly bent due to the sharp $M_b(H_b)$ rise concomitant with the **d**-vector rotation to follow $M_b(H_b)$ shown by the green line in Fig. 15. Since $M_b(H_b)$ starts at the temperature T_{c0} midway between T_{c1} and T_{c2} separated by $2M_c$, the second transition temperature T_{c2} is found to locate there where the A_2 phase begins developing while the remaining large region is occupied by the A_1 phase. Now we see the multiple phases in this situation, which are absent under the ambient pressure in URhGe. We can estimate the spontaneous moment M_c under $\sigma = 1.0$ GPa as $M_c = 0.06\mu_B$ on the simple assumption that κ is unchanged under the uniaxial pressure.

We analyze the experimental data available under uni-axial pressure [75] displayed in Fig. 16. It is seen the continuous and systematic evolution of the multiple phase diagrams under uniaxial pressure. Namely, as uniaxial pressure σ increases, three characteristic temperatures T_{c1}, T_{c0}, and T_{c2} shift together to higher temperatures. T_{c2} appears at a finite temperature ($T > 0$) around $\sigma \sim 0.8$ GPa, keeping to move up with increasing further σ. The separation of T_{c1} and T_{c2} becomes narrow because the spontaneous moment M_c gets diminished, corresponding to the observed Curie temperature decrease under uniaxial pressure [75] [see Fig. 17(b)].

We show the changes of three temperatures T_{c1}, T_{c0}, and T_{c2} assigned thus in Fig. 17(a). The separation between T_{c1} and T_{c2} determined by M_c diminishes simply because M_c decreases as σ increases. This results in $T_{c2} > 0$ appearing above $\sigma > 0.8$ GPa, where the double transitions at $H = 0$ should be observed. It is remarkable to see that upon approaching $\sigma = 1.2$ GPa from below, all the transition temperatures are converging toward $\sigma_{cr} = 1.2$ GPa. This means that above this pressure, the genuine symmetric A phase is realized because the symmetry-breaking parameter M_c vanishes where the spin symmetry of the pair function restores SO(3) full symmetry,

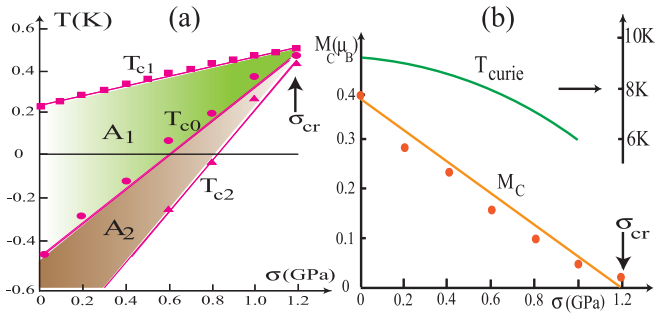

FIG. 17. (a) The resulting T_{c1}, T_{c0}, and T_{c2} obtained from the analysis in Fig. 16 are displayed. The linear changes of those characteristic temperatures T_{c1}, T_{c0}, and T_{c2} are found, corresponding to the linear decrease in M_c. The second transition T_{c2} begins appearing above $\sigma > 0.8$ GPa where the double transitions are expected at $H = 0$. (b) The resulting M_c change as a function of uniaxial pressure σ. The observed Curie temperatures (Ref. [75]) are also shown. It is consistent with the obtained decreasing tendency of M_c as σ increases.

a situation similar to that shown in Fig. 1 (also see Fig. 25 later). At the critical pressure $\sigma_{cr} = 1.2$ GPa the pairing state is analogous to the superfluid ^{3}He-A phase.

The resulting analysis of the spontaneous moment M_c is shown in Fig. 17(b), revealing a monotonous decrease as σ increases. This tendency is matched with the lowering of the Curie temperature, which is observed experimentally [75]. It is interesting to see the linear changes of T_{c1}, T_{c0}, T_{c2}, and M_c near the critical uniaxial pressure $\sigma_{cr} = 1.2$ GPa. This linear relationship is similar to those in UTe_2 under hydrostatic pressure around the critical pressure $P_{cr} = 0.2$ GPa (see Fig. 25 later).

E. UCoGe

UCoGe is another ferromagnetic superconductor worth checking our theory in the same framework for URhGe. Major differences from URhGe in the previous section lie in the fact that (1) the small spontaneous moment $M_c = 0.06\mu_B$; (2) the field-induced moments of M_b and M_a in the hard axes are comparable in magnitude as shown in Fig. 8(a); (3) the magnetization rotation field $H_R \sim 45$ T is far above H_{c2}. Those are contrasted with URhGe with the distinctive induced moment for M_b that ultimately leads to the RSC. However, H_{CR} is situated at low fields 6 ∼ 8 T in UCoGe.

1. $H \parallel b$: S-shaped H_{c2} and multiple phases

In Fig. 18 we show the result for the phase diagram in $H \parallel b$, assuming that $\kappa = 1.8\frac{K}{\mu_B}$. The two transition temperatures T_{c1} and T_{c2} are split by $M_c = 0.06\mu_B$. Under the applied field H_b, the spontaneous moment $M_c(H_b)$ decreases. T_{c1} and T_{c2} approach each other to meet at $H^b_{CR} \sim 6$ T. Before meeting there, the upper $T_{c1}(H_b)$ increases and follows the magnetization $M_b(H_b)$ by rotating the **d**-vector direction from the c-perpendicular direction to the b-perpendicular direction. This results in an S-shaped H_{c2} curve which eventually reaches H^{AUL}_{c2}, giving the extrapolated $H^b_{c2} \sim 25$ T. We notice here that the initial slope of H^b_{c2} is small, extrapolated to H^b_{c2}

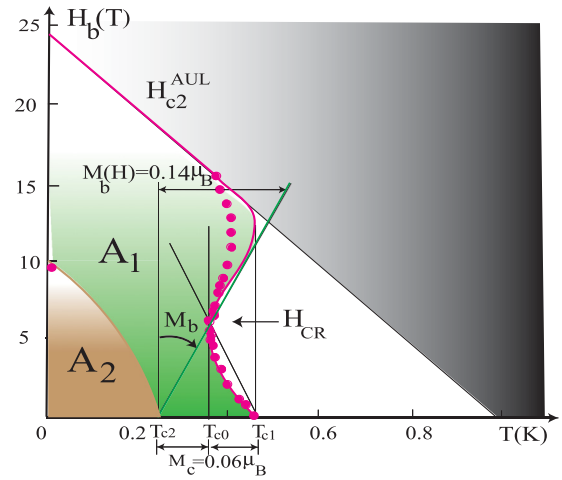

FIG. 18. The S-shaped phase diagram for UCoGe in $H \parallel b$. H^b_{c2} starts at T_{c1} and is initially depressed by the orbital depairing. At around the crossing field H_{CR} it turns toward higher T due to the **d**-vector rotation to follow $M_b(H_b)$ denoted by the green line, forming the S shape. At further high fields after hitting H^{AUL}_{c2}, H^b_{c2} follows it. The experimental data points come from [40] and the point at $T = 0$ and 10 T from [62].

less than a few T, which is comparable to $H^c_{c2} \sim 0.5$ T. This means that the intrinsic H_{c2} anisotropy is within the range of the usual effective mass anisotropy. The same nearly isotropic H_{c2} behavior was just emphasized in URhGe (see Fig. 13). The superficial H_{c2} anisotropy with the order of $H^b_{c2}/H^c_{c2} = 25$ T/0.5 T ∼ 50 is an artifact due to ignoring the origin of the S-shaped H^b_{c2}. This is often pointed out as one of the major mysteries in UCoGe [5].

It is important to notice that because we identify $T_{c2} = 0.2$ K there must exist the phase boundary of A_1 and A_2 phases. According to thermal-conductivity measurement in Ref. [62] as a function of H_b, there indeed exists an anomalous thermal-conductivity jump at 10 T and low T indicated as the red dot on the H axis in Fig. 18. This nicely matches our identification of the A_2 phase boundary line, a situation similar to the characteristics in Figs. 4(c) and 5(b). This assignment is consistent with the H^c_{c2} phase diagram as shown shortly.

2. $H \parallel a$

As already shown in Fig. 8(a), the magnetization curves of M_b and M_a are quite similar. The crossing field H^i_{CR} ($i = a$ and b) at which $M_b(H_b)$ and $M_a(H_a)$ reach $M_c = 0.06\mu_B$ is seen to be $H^a_{CR} \sim 8$ T and $H^b_{CR} \sim 6$ T. Thus, H^a_{c2} curve is anticipated to be similar too. Indeed the result is shown in Fig. 19(a). Even though the S-shaped H^b_{c2} is weakened, it is still seen as a weak anomaly at around $H^a_{CR} \sim 8$ T which is a signature that $T_{c1}(M)$ in Eq. (26) follows $M_a(H_a)$ by rotating the **d** vector whose direction is perpendicular to the c axis. It is now perpendicular to the a axis. We also point out that the A_1 and A_2 phase diagrams are essentially the same as in $H \parallel b$ and the extrapolated $H^a_{c2} \sim 22$ T is comparable to $H^b_{c2} \sim 25$ T.

3. $H \parallel c$ and multiple phases

We display the analysis for the phase diagram in $H \parallel c$ in Fig. 19(b). The existing experimental data clearly indicate

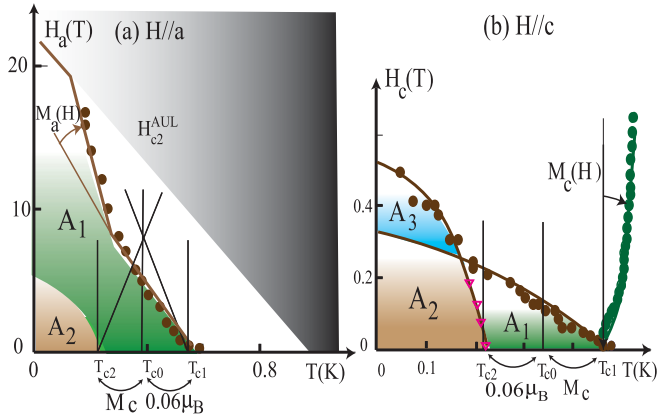

FIG. 19. (a) Weakened S shape H_{c2}^{a} for $H \parallel a$ in UCoGe because H_{CR} moves up compared to H_{c2}^{b} case shown in Fig. 18. The data are from Ref. [40]. (b) H_{c2}^{c} for $H \parallel c$ in UCoGe. The data [62] clearly show the anomaly around 0.3 T, indicating the multiple phases identified as A_1, A_2, and A_3. The magnetization curve of $M_c(H_c)$ is displayed as the green dots, showing the weak rise in this scale. Both H_{c2}^{c} starting at T_{c1} and T_{c1} are thus dominated by the orbital depairing without help of the magnetization. The four points denoted by the red triangles are read off from the thermal-conductivity anomalies [76].

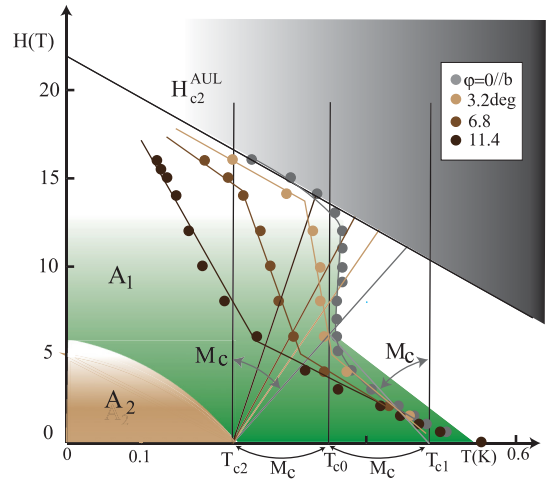

FIG. 20. $H_{c2}(\phi)$ for $\phi = 0°$, 3.2°, 6.8°, and 11.4° from the b axis toward the a axis in UCoGe. The data are from Ref. [40]. As ϕ increases, M_c grows slowly as a function of H (the counterclockwise rotation of the M_c curves), pushing up H_{CR} to higher fields. This results in the decrease of $H_{c2}(\phi)$ because the orbital suppression becomes dominant. The enhanced H_{c2} becomes diminished as ϕ increases.

that H_{c2}^{c} consists of the two parts where the H_{c2}^{c} enhancement is visible at low T and high H. Thus, the phase diagram is divided into the three phases A_1, A_2, and A_3, where A_3 is genuine spin down-down pair while A_2 is a mixture of up-up and down-down pairs, or a distorted A phase with different population of the two spin pairs.

As indicated in Fig. 19(b) as the green dots, the magnetization curve of $M_c(H_c)$ is weakly increasing in this scale. Thus, the slope at T_{c1} is exclusively governed by the orbital depairing, implying that this comes from the effective mass along the c axis. The anisotropy of the initial slopes in H_{c2} at T_{c1} is determined by their effective mass anisotropy.

4. Rotation ϕ from the b axis toward the a axis

Finally, we touch upon the case of the field rotation from the b axis toward the a axis by ϕ as shown in Fig. 20. As H is turned from the b axis toward the other hard a axis, the crossing field H_{CR} increases as shown in Fig. 8(a). Since $M_c(H)$ becomes slowly increasing as H increases, the orbital depression gets stronger and flattens the initial slopes of $H_{c2}(\phi)$ at T_{c1}, eventually approaching H_{c2}^{a} as shown in Fig. 19(a). This is already realized in the $\phi = 11.4°$ case seen from it. It should be pointed out again that those initial slopes at T_{c1} for those ϕ values only slightly change, implying that the initial slope is determined by the effective masses, namely, the orientational-dependent Fermi velocities.

So far we assumed that $\kappa = 1.8$ K$/\mu_B$ under the condition of the existence of the second transition $T_{c2} = 0.2$ K. But we are warned that if those suggestive signatures of the second phase A_2 coming from thermal-conductivity measurements [62,76] may be an artifact, then the forgoing arguments go through and are almost unchanged by taking $\kappa = 3.6$ K$/\mu_B$ without the A_2 phase. Namely, we are still in ambiguous situations to finally pin down the system parameters. Therefore, it is urgent to confirm or refute the existence of the second transition in order to go further from here.

F. UTe_2

To coherently explain a variety of physical properties of superconducting state in UTe_2 accumulated experimentally in the same context of the other compounds, URhGe and UCoGe, we need a basic assumption that the ferromagnetic fluctuations are slow enough compared to the electron motion of the conduction electrons, which condense at T_c. The slow FM fluctuation moments characterized by the nonvanishing square root-mean averaged value $\sqrt{\langle(\delta M_a)^2\rangle}$ over time and space $\langle \dots \rangle$ are assumed to be able to break the spin symmetry SO(3) of the Cooper pairs. In the following we denote this spontaneous and instantaneous FM moment simply $M_a = \sqrt{\langle(\delta M_a)^2\rangle}$, whose magnitude is adjusted in order to best reproduce the H_{c2} phase diagram as we will see next.

1. H ∥ b axis

We follow the same method for URhGe and UCoGe to understand the observed L-shaped H_{c2}^{b} applied to the magnetic hard b axis. Here we assume that $M_a = 0.48\mu_B$ and $\kappa = 6.9K/\mu_B$. As seen from Fig. 21, H_{c2}^{b} starts from $T_{c1} = 1.6$ K, following $M_a(H_b)$ which decreases with increasing H_b toward H_{CR}. H_{CR} is roughly estimated from the magnetization curves shown in the inset of Fig. 8(b) as around 20 T. Above $H_b > H_{CR}$ the **d** vector rotates in order to follow the magnetization $M_b(H_b)$, which strongly increases from T_{c0}. H_{c2}^{b} begins following it to grow and forms the upper part of the L shape. It eventually reaches $H_R = 32$ T where the first-order transition occurs. As shown in the inset of Fig. 8(b) the magnetization jump at H_R amounts to $0.6\mu_B$ known experimentally [14]. The reached magnetization (the horizontal green line) is deep outside H_{c2}^{AUL} shown by dark black colored

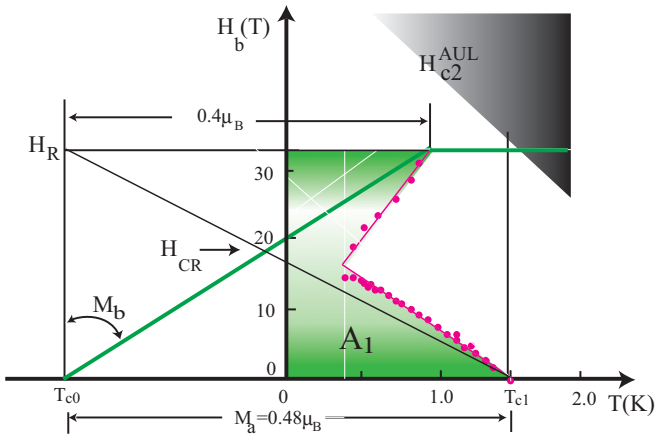

FIG. 21. The L-shaped H_{c2}^{b} observed in [12] is shown (red dots). H_{c2}^{b} starting at T_{c1} follows the orbital suppression plus the M_a depression by H_b toward H_{CR}. When it approaches the strong increasing $M_b(H_b)$, the **d** vector rotates and follows $M_b(H_b)$ to grow. This forms the upper part of the L shape. In further high fields H_{c2}^{b} reaches $H_R = 32$ T and disappears there by hitting H_{c2}^{AUL}. The green curve denotes the magnetization curve $M_b(H_b)$ shown in the inset of Fig. 8(b) [14].

region in Fig. 21. Therefore, H_{c2}^{b} simply stops when it hits the H_R line. Those features nicely reproduce the experimental characteristics shown in Fig. 21.

2. ϕ rotation from the b axis toward the a axis

When the field tilts from the b axis toward the magnetic easy a axis by the angle ϕ, the magnetization $M_b(H_b)$ growth becomes slow compared to that for the b axis as shown in Fig. 22. Those counterclockwise changes of $M_b(H_b)$ for various angle ϕ in Fig. 22 are estimated by the method explained

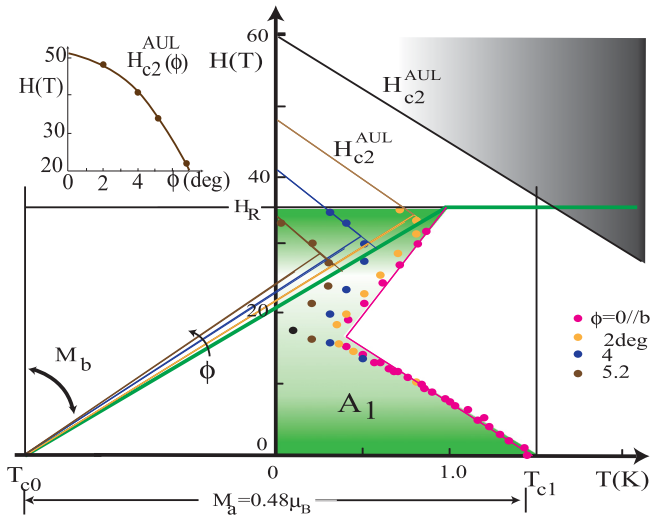

FIG. 22. $H_{c2}(\phi)$ for $\phi = 0°$, $2°$, $4°$, $5.2°$, and $6.3°$ from the b axis toward the a axis. $M_b(H)$ grows slowly with increasing ϕ. $H_{c2}(\phi)$ curves bent over. Before hitting $H_R(\phi)$ which ultimately limits it, $H_{c2}(\phi)$ turns around with the negative slope because they reach their own $H_{c2}^{AUL}(\phi)$. $M_b(H)$ for each ϕ is estimated by Eq. (25). The data (dots) are from [12]. The inset shows $H_{c2}^{AUL}(\phi)$ estimated by extrapolating the straight lines toward higher fields beyond $H_R(\phi)$.

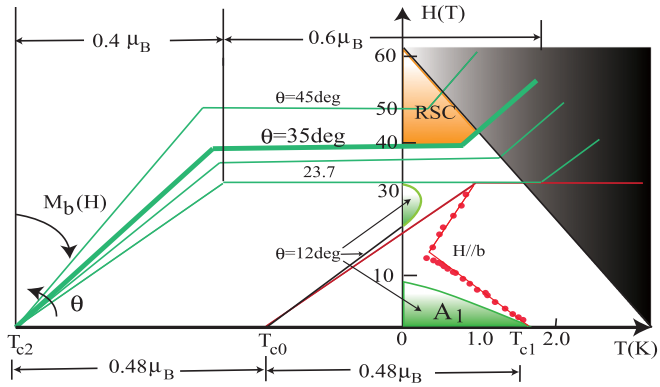

FIG. 23. $H_{c2}(\theta)$ for various θ, which are measured from the b axis toward the c axis. The magnetization curves of $M_b(H)$ starting at T_{c2} and T_{c0} evaluated before [see Fig. 8(b)] lead to the reentrant SC for $\theta = 35°$ in addition to the low H_{c2}. For the lower angle of $\theta = 12°$ the two separate SC are formed. Here the $\theta = 0°$ case ($H \parallel b$) is shown for reference. It is seen that the magnetization curves only around $\theta \sim 35°$ allow RSC to appear.

in Sec. IV. Therefore, H_{c2} is bent upward in the upper part of their L-shaped ones while the lower parts are hardly changed because this is mainly limited by the orbital suppression. Those $H_{c2}(\phi)$ curves for various ϕ values eventually reach their own H_{c2}^{AUL} which depends on ϕ, followed by the orbital suppression. Then, $H_{c2}(\phi)$ finally disappears abruptly by hitting $H_R(\phi)$. If those $H_{c2}(\phi)$ curves extrapolate naively to higher fields beyond $H_R(\phi)$, we find $H_{c2}^{AUL}(\phi)$ as shown in the inset of Fig. 22, indicating that $H_{c2}^{AUL}(\phi)$ changes strongly within a few degrees, peaking at $H \parallel b$ sharply. We are not able to explain this peaking phenomenon at this moment. A similar peaking phenomenon is also observed in the θ side too, where the $H_{c2}(\theta)$ peak occurs at $\theta \sim 35°$.

Thus, the SC region in the ϕ-H plane is quite limited to small angles up to $\phi \sim 6.3°$. As will show next, this is similar to the θ case where the high field SC $H_{c2}(\theta \sim 35°) = 60$ T is observed in a narrow angle θ region above $T_R(\theta)$.

3. θ rotation from the b axis toward the c axis

It is remarkable to see the extremely high $H_{c2}(\theta = 35°) \sim 60$ T when the field is tilted from the b axis toward the other magnetic hard c axis [15]. This is detached from the low field $H_{c2}(\theta) \sim 8$ T. This low field SC part is nearly independent of θ. This H_{c2} isotropy was seen also in URhGe (see Fig. 13) and UCoGe. This extremely high $H_{c2}(\theta = 35°)$ can be understood by the present framework as follows.

We begin with the $H \parallel b$ case discussed in Fig. 21. Upon increasing θ, the magnetization $M_b(H)$ becomes slow to grow. Around $\theta = 12°$ the upper part of the L-shaped H_{c2} separates into two parts as shown in Fig. 23 which is observed [77]. Eventually this RSC part disappears above $\theta > 12°$, leaving only the lower H_{c2} part at around 10 T.

Further increasing θ, the magnetization $M_b(H)$ starting from T_{c2} becomes relevant because as explained in Fig. 8(b), $M_b(H)$ becomes small and the magnetization jump also diminishes. Around $\theta = 35°$ the magnetization curves are just available for the reentrant SC to appear at higher fields above the respective $H_R(\theta)$. This RSC is shown in Fig. 23. This is

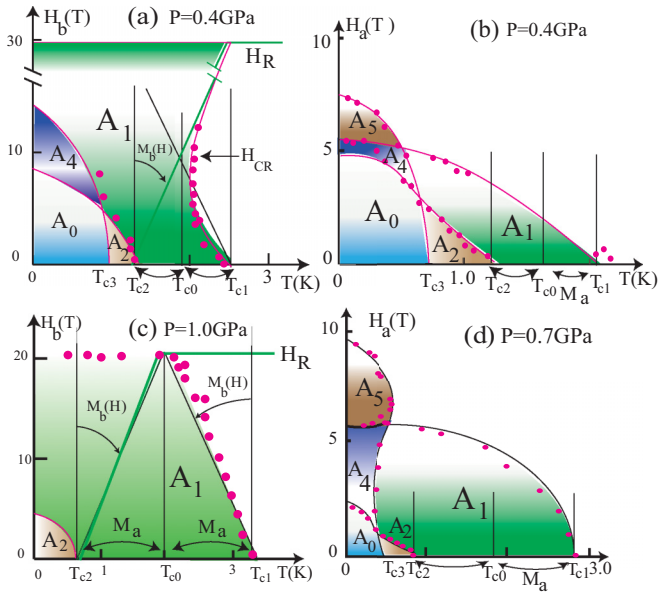

FIG. 24. H_{c2} and the associated internal phase transition lines under hydrostatic pressure P in UTe_2. (a) $P = 0.4$ GPa and $H \parallel b$. (b) $P = 0.4$ GPa and $H \parallel a$. (c) $P = 1.0$ GPa and $H \parallel b$. (d) $P = 0.7$ GPa and $H \parallel a$. The data denoted by the red dots are from Ref. [28]. T_{c1} and T_{c2} at $H = 0$ are split by the magnetization M_a which decreases under the applied field H_b as shown in (a) and (c). This decrease of $M_a(H_b)$ is compensated by growing of the magnetization $M_b(H_b)$ as denoted by the green lines there.

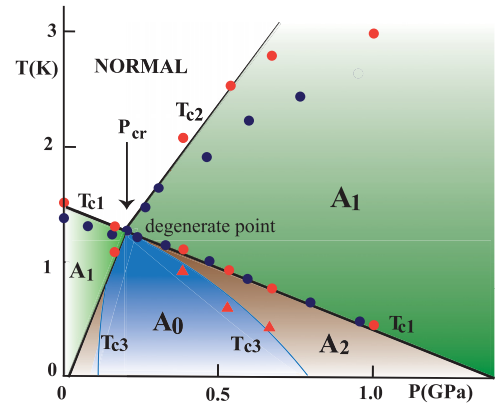

FIG. 25. T-P phase diagram in UTe_2 with three transition temperatures T_{c1}, T_{c2}, and T_{c3} corresponding to the A_1, A_2, and A_0 phases, respectively. At the degenerate point of $P_{cr} = 0.2$ GPa all three phases converge. The lines for T_{c1} and T_{c2} as a function of P indicate that the underlying symmetry-breaking field M_a changes linearly with P, leading to the globally quadratic variation of T_{c3} from the degenerate point. The red (dark blue) round dots are from the experiment [28] ([13]) except for the three red triangle points at $P = 0.40$, 0.54, and 0.70 GPa for T_{c3}, which are inferred from Fig. 24.

because the state reached after the first-order jump is now within the H_{c2}^{AUL} allowed region. Thus, RSC only appears within the narrow angle region centered at $\theta = 35^\circ$. Those RSC regions are characterized by a trianglelike shape as observed in [15]. This RSC shape resembles those in Figs. 9 and 10 for URhGe.

4. Phase diagrams under pressure and multiple phases

Let us examine the pressure effects on the H_{c2} phase diagram, which give us another testing ground to check the present scenario. In Fig. 24(a) we show the data (dots) of H_{c2}^b for $H \parallel b$ under $P = 0.4$ GPa [28] together with our analysis. It is seen that since the magnetization curve $M_b(H_b)$ denoted by the green line strongly increases, H_{c2}^b started at T_{c1} exhibits a bent toward higher temperatures at around H_{CR}. The two magnetization curves started from T_{c1} and T_{c2} meet at H_{CR}. After passing the field H_{CR}, H_{c2}^b with a positive slope heads toward $H_R = 30$ T, which is observed as the first-order transition [28]. The same feature is observed so far several times in URhGe under uniaxial pressure such as in Fig. 15 and UCoGe in Fig. 18.

The second transition at T_{c2} with the A_2 phase is clearly found experimentally shown there detected by AC calorimetry by Aoki *et al.* [28]. Moreover, the lower H_{c2}^b started from T_{c2} shows an anomaly at around 5 T in Fig. 24(a), suggesting the third transition T_{c3}. This identification is quite reasonable when we see Fig. 24(b) where the $H \parallel a$ case is displayed for the same $P = 0.4$ GPa. Indeed, we can consistently identify T_{c3} in this field orientation too. According to our theory, three phases A_1, A_2, and A_0 correspond to T_{c1}, T_{c2}, and T_{c3}, respectively, as shown there. In the high fields, we enumerate further phases A_4 and A_5. Those lower T and high H phases are the mixtures of the fundamental three phases A_1, A_2, and A_0 except for A_5, which is genuine A_0. For example, the A_4 phase consists of the A_1 and A_0 phases.

In Fig. 24(c) we show the data of H_{c2}^b for $H \parallel b$ under $P = 1.0$ GPa [28] together with our analysis. As P increases, the first-order transition field H_R becomes lower: Here it is $H_R = 20$ T at $P = 1.0$ GPa from 30 T at $P = 0.4$ GPa. H_{c2}^b just follows a straight line due to the orbital depairing all the way up to H_R where the magnetization $M_b(H_b)$ denoted by the green line exhibits the magnetization jump. This jump is large enough to wipe out the SC state there. Thus, H_{c2}^b now follows a horizontal line at $H_R = 20$ T. This is the same case as in H_{c2}^b seen in the ambient pressure (see Fig. 21). The main difference from the ambient case is that the second transition at T_{c2} is now visible and observable because the FM moment M_a diminishes under pressure and the pressure $P = 0.4$ GPa is situated near the critical pressure at $P = 0.2$ GPa (see Fig. 25). This proves the consistency of our scenario.

As shown in Fig. 24(d) where at $P = 0.7$ GPa for $H \parallel a$ the H_{c2} data points are quoted from Ref. [28], we draw the three continuous lines to connect those points. We find the missing third transition along the T axis at $T_{c3} = 0.5$ K. Note that the tricritial point with three second order lines is thermodynamically forbidden [78]. The multiple phases are enumerated, such as A_1, A_2, and A_0 at the zero field and A_4 and A_5 at finite fields. Those phases are consisting of the coexistence of the plural fundamental three components A_1, A_2, and A_0. Namely, those are characterized by A_1 at T_{c1}, $A_2 \to A_1 + A_2$ at T_{c2}, $A_0 \to A_1 + A_2 + A_0$ at T_{c3}, $A_4 \to A_1 + A_0$, and $A_5 \to A_0$. It is understood that this phase diagram is quite exhaustive, and no further state is expected in our framework. At the intersection points in Fig. 21(d) the four transition lines should

TABLE II. Possible pairing functions.

Compound	Spin part	Orbital part $\phi(k)$
URhGe	$\vec{a} \pm i\vec{b}$	$k_a k_b k_c(A_{1u})$, $k_b(B_{1u})$, $k_c(B_{2u})$, $k_a(B_{3u})$
UCoGe	$\vec{a} \pm i\vec{b}$	$k_a k_b k_c(A_{1u})$, $k_b(B_{1u})$, $k_c(B_{2u})$, $k_a(B_{3u})$
UTe_2	$\vec{b} \pm i\vec{c}$	$k_b + ik_c$

always meet together according to the above general rule and thermodynamic considerations [78]. T_{c3} could be raised by the presence of the A_1 and A_2 phases due to the fourth-order term $\mathrm{Re}(\eta_a^2\eta_+\eta_-)$ mentioned in Sec. II.

In Fig. 25 we compile all the data [13,28] of the phase transitions in the T-P plane at $H = 0$. As P increases from $P = 0$, T_{c1} (T_{c2}) decreases (increases) to meet at the critical pressure $P_{cr} = 0.2$ GPa where T_{c3} is also merging to converge all three transition lines. This critical pressure corresponds to the degenerate point where the symmetry-breaking parameter M_a vanishes and the three phases A_1, A_2, and A_0 become degenerate, restoring the full SO(3) spin symmetry at this critical point. Upon further increasing P, the three phases are departing from there. The three data points for T_{c3} (the three red triangles on the T_{c3} line in Fig. 25) are inferred from Fig. 24. The fact that T_{c1} and T_{c2} behave linearly in P is understood as the linear relationship between P and $M_a(P)$, leading to the linear changes of T_{c1} and T_{c2}. This linear relationship is also seen in Fig. 17. Simultaneously, a strong departure of T_{c3} comes from the critical pressure. This is because T_{c3} changes in proportion of M_a^2 [see Eq. (26)]. This T-P phase diagram is similar to that shown in Fig. 1 globally and topologically, proving that the present scenario is valid for this compound too.

VI. PAIRING SYMMETRY

A. Gap symmetries and nodal structures

The classification of the gap or orbital symmetries allowed in the present orthorhombic crystal has been done before [49,56]. Among those classified pairing states, the appropriate gap function $\phi(k)$ is selected as follows: $\phi(k) = k_a k_b k_c$ (A_{1u}), $\phi(k) = k_b$ (B_{1u}), $\phi(k) = k_c$ (B_{2u}), and $\phi(k) = k_a$ (B_{3u}). The gap structure is characterized by the line nodes for those states. They are all candidates for URhGe and UCoGe as tabulated in Table II. This leads to the overall pairing function $\mathbf{d}(k) = (\vec{a} \pm i\vec{b})\phi(k)$, which breaks the time-reversal symmetry. This gap structure with the line nodes is consistent with the NMR experiment [41], reporting that $1/T_1$ is proportional to T^3 at low temperatures. The line nodes are also suggested by other experiments on UCoGe [62,76]. Note that the spin part and orbital part are independent in our weak SOC scenario.

As for UTe_2, the specific-heat experiments [9,10,16,29] exhibit $C/T \sim T^2$, suggesting that the gap structure is characterized by point nodes. This is also consistent with the microwave measurements [22]. Then we have to resort to an *ad hoc* orbital function, namely, $\phi(k) = k_b + ik_c$, beyond the group-theoretical classification scheme [47,48], thus the resulting overall pairing function is given by $\mathbf{d}(k) = (\vec{b} \pm i\vec{c})(k_b + ik_c)$. This pairing state is also the time-reversal broken state both in spin and orbital parts. The point nodes are oriented along the a axis determined by angle-resolved specific-heat experiment [29]. This is characterized by the Weyl nodes analogous to superfluid ^{3}He-A phase [79,80]. This double chiral state both in the spin space and orbital space might be energetically advantageous because the spin and orbital moments for Cooper pairs are parallel, namely, the orbital angular moment $\mathbf{L}$ that is spontaneously induced by this chiral state can gain the extra energy through the coupling $\mathbf{M}_s \cdot \mathbf{L}$ with the spontaneous magnetic moment $\mathbf{M}_s \propto \mathbf{d}\times\mathbf{d}^*$. This is consistent with the experiments by angle-resolved specific-heat measurement [29], the STM observation [17], and the polar Kerr experiment [21], among other thermodynamic experiments [20].

B. Residual density of states

All the compounds exhibit more or less the residual density of states at the lowest-T limit in the specific-heat measurements [5,29]. This is not a dirt effect of the samples used, but it is intrinsic deeply rooted to the pairing state identified as the A_1 phase. In the A_1 phase the superconducting DOS has intrinsically the "residual density of states." Since T_{c1} with the A_1 phase is higher than T_{c2} with the A_2 phase, it is reasonable to expect the the DOS $N_{A_1}(0)$ in the A_1 phase is larger than that in the A_2 phase, that is,

$$N_{A_1}(0) > N_{A_2}(0)$$

because in the Zeeman split bands, the major spin component band with larger DOS preferentially forms the higher-T_c superconducting state rather than the minority band. It is quite reasonable physically that in UTe_2 at the ambient pressure the observed "residual density of states" corresponding to $N_{A_2}(0)$ is less than 50%.

C. Multiple phase diagram

Our three-component spin-triplet state leads intrinsically and naturally to a multiple phase diagram consisting of the A_0 phase at T_{c3}, A_1 at T_{c1}, and A_2 at T_{c2} as shown in Fig. 1 under nonvanishing symmetry-breaking field due to the spontaneous moment. Depending on external conditions, such as T, H, and its direction, or pressure, etc., the structure of the multiple phase diagram is varied as explained. In fact, under P, the successive double transitions are clearly observed in UTe_2 [13] and they vary systematically in their P-T phase diagram of Fig. 25. We see even the third transition centered around the critical pressure $P_{cr} = 0.2$ GPa. At the ambient pressure on UTe_2 the occurrence of the second transition is debated [21,26], including the detailed internal phase lines. But they agree upon the existence of the multiple phases.

As for UCoGe, the thermal-conductivity experiment [76] indicates an anomaly at $T = 0.2$ K, which coincides roughly with our prediction shown in Figs. 18 and 19. As a function of $H(\parallel b)$, the thermal-conductivity anomaly is detected as a sudden increase at $H \sim 0.6H_{c2}$ (see Fig. 5 in Ref. [73]). Moreover, under H parallel to the easy c axis, the H_{c2} curve in Fig. 19(b) shows an enhancement at low T indicative of the underlaying phase transition [see Fig. 2(b) in Ref. [62]]. According to the NMR by Manago *et al.* [41,42], $1/TT_1$ presents a similar T behavior, such as a plateau at $\sim N(0)/2$ and then a

sudden drop upon lowering T. We propose to conduct further careful experiments to detect the A_1-A_2 transitions in this compound.

In URhGe at the ambient pressure shown in Fig. 9 both low field phase and the RSC phase belong to the A_1 phase. However, under the uniaxial pressure along the b axis, there is a good chance to observe the second transition as explained in Figs. 15 and 16.

Therefore, to confirm the generic multiple phase diagram for all three compounds shown in Fig. 1 is essential to establish the present scenario and also to detect characteristics of each pairing state associated with those multiple phases.

D. Symmetry-breaking mechanism

For URhGe and UCoGe the "static" FM transitions are firmly established, and there is no doubt for the spontaneous FM moment to be a symmetry-breaking field. Slow FM fluctuations are found in UTe_2 [9,14,18,19] which could be the origin of the symmetry breaking of $T_{c1} \neq T_{c2}$ under the assumption that FM fluctuations are slow compared to the conduction electron motion. A similar observation is made in UPt_3: The fluctuating antiferromagnetism (AF) at $T_N = 5$ K is detected only through the fast probe: "nominally elastic" neutron diffraction [81,82] and undetected through other "static" probes, such as specific heat, μSR, and NMR. Thus, the AF fluctuating timescale is an order of MHz or faster. This is believed to be the origin of the double transition in UPt_3 [83,84].

In UTe_2 it is essential and urgent to characterize the observed ferromagnetic fluctuations in more detail, such as fluctuation timescale or spatial correlation. Elastic and inelastic neutron scattering experiments are ideal tools for it, which was the case in UPt_3. It may be too early to discuss the pairing mechanism before confirming the nonunitary spin-triplet state. There already exists an opinion [85] which advocates longitudinal ferromagnetic fluctuations to help stabilizing a spin-triplet state before the discoveries of those compounds. A problem of this sort is how to prove or refute it, otherwise, it is not direct evidence and remains only a circumstantial one. We need firm objective "evidence" for a pairing mechanism.

E. Common and different features

As already seen, URhGe, UCoGe, and UTe_2 are viewed coherently from the unified point: The nonunitary triplet state. They share the following common features: (1) The unusual H_{c2} curves occur for the field direction parallel to the magnetic hard b axis, where the magnetization curve $M_b(H_b)$ exhibits the first-order transition at H_R for URhGe and UTe_2, corresponding to the FM moment rotation. (2) Under pressure they show the critical point behaviors $P_{cr} = 0.2$ GPa for UTe_2 and $\sigma_{cr} = 1.2$ GPa for URhGe at which the split T_{c1} and T_{c2} converges, leading to the SO(3) spin symmetry for Cooper pairs. (3) The multiple phases, including the reentrant SC, are observed and explained in URhGe and UTe_2 and expected to be confirmed for UCoGe. (4) The GL parameter κ characterizing the strength of the symmetry breaking is tabulated in Table I, showing the similar values for three compounds. As a general tendency, κ is likely larger when the FM moment is larger because it is originated from the particle-hole asymmetry of the density of states $N(0)$ at the Fermi level.

There are two different features: (1) The nodal structures are points oriented along the magnetic easy a axis in UTe_2 while lines in URhGe and UCoGe. (2) Under the ambient pressure, H_{c2} curves are seemingly different as in Fig. 9 for URhGe, Fig. 18 for UCoGe, and Fig. 21 for UTe_2. But it is now understood as mere differences in T_{c0} or the FM moments as the symmetry breaker.

From this comparison, the superconductivity in UTe_2, URhGe, and UCoGe should be understood by the unified viewpoint, which is more resourceful and productive than considered differently and individually.

F. Double chiral nonunitary state in UTe_2

Since UTe_2 attracts much attention currently, it is worth summing up our thoughts on this system to challenge novel experiments. When combining the experimental observations of the chiral current along the wall by STM [17] and the angle-resolved specific-heat experiment [29], the double chiral nonunitary symmetry described by $\mathbf{d}(k) = (\hat{b} + i\hat{c})(k_b + ik_c)$ is quite possible: This pairing state produces the chiral current at the edges of domain walls, consistent with the former observation. And it is consistent with the polar Kerr experiment [21] which shows the broken time-reversal symmetry. In this pairing state the point nodes orient along the magnetic easy a axis, which is supported by the angle-resolved specific-heat experiment [29]. This experiment further indicates the unusual Sommerfeld coefficient $\gamma(H)$ in the superconducting state for H along the a axis. The low-energy quasiparticle excitations naively expected for the point nodes [86] are absent. This lack of the nodal excitations is understood by taking into account that T_c depends on H through the magnetization. This is indeed consistent with the notion of the field-tuned SC developed throughout this paper.

G. Rotation of d vector observed in UTe_2

Throughout the paper we have assumed that the spin-orbit coupling (SOC) is not in the strong coupling limit which prohibits the **d**-vector rotation due to the strong locking to lattices. In contrast, in a finite SOC case the **d** vector reorients under the action of magnetic fields. It is true that SOC in the single-particle level is strong in those U-based heavy-fermion superconductors, which play key roles in understanding various magnetic properties, such as magnetic anisotropy. Since one-body SOC is already taken into account to the formation of the band structure, etc., the resultant effective SOC in the many-body level acting for the Cooper pairs is different from it. Generically, it is finite whose magnitude depends on situation. But the weak SOC, or more precisely finite SOC, is a conjecture in this paper.

Then, the **d**-vector rotation phenomena have been discussed in connection with various spin-triplet superconductors, such as UPt_3 [60,87], UBe_{13} [88], its candidates Sr_2RuO_4 [89,90], and also with heterostructures [91–94]. For UPt_3 the c-axis external field around a few kG has been observed to reorient the **d** vector through the Knight shift experiments [95].

The recent observation of the **d**-vector rotation in UTe_2 [54,55] by the Knight shift experiments at around $H \parallel c \sim 5$ T [54] and $H \parallel b \sim 12.5$ T [55] is a direct manifestation that the effective SOC is finite. In particular, $H_{CR} \parallel b$ shown in Fig. 21 approximately agrees with the latter observation. The former is somewhat unexpected, but shows that the strength of the SOC is small.

VII. SUMMARY AND CONCLUSION

We have discussed the superconducting properties of URhGe, UCoGe, and UTe_2 in detail in terms of a nonunitary spin-triplet pairing state in a unified way. The spontaneous static ferromagnetic moment in URhGe and UCoGe, and the slowly fluctuating instantaneous ferromagnetic moment in UTe_2, break the spin SO(3) symmetry in the degenerate triplet pairing function with three components. Those produce the various types of the H_{c2} curves that are observed. The possible pairing function is described by the complex **d** vector, whose direction is perpendicular to the magnetic easy axis at zero field. Its direction changes under applied field parallel to the magnetic hard b axis common in three compounds. This **d**-vector rotation is driven by the induced magnetic moment under applied fields. Thus, the SC order parameter is tunable by the magnetic field in this sense, ultimately leading to the reentrant SC in URhGe, S shape in UCoGe, and L shape H_{c2} in UTe_2.

As for UTe_2, we can study a variety of topological properties, such as Weyl nodes associated with the point nodes, known in ^{3}He -A phase [79,80], which was difficult to access experimentally and remains unexplored in the superfluid ^{3}He. We can hope to see in UTe_2 similar exotic vortices and Majorana zero modes predicted in ^{3}He phase [79,80,96,97]. Specifically, (1) Majorana zero modes, or the fermion zero modes [98], exist in this chiral superconductor, either at the boundary edges or the vortex core as the zero-energy bound state. (2) Half-quantum vortex: There are several exotic vortices, which are different from the conventional singular Abrikosov vortex with the unit winding number, associated with the $(b + ic)(p_b + ip_c)$ pairing. The half-quantum vortex with the half-winding number is expected to be stabilized where the spin and orbital components with the half-quantized winding are responsible for the total unit winding [99,100]. (3) Skyrmion: The Mermin-Ho vortex or the so-called skyrmion may be stabilized under certain conditions [101]. It is known that the Majorana zero modes do not exist in this Mermin-Ho vortex, which is a nonsingular vortex. (4) Vortex lattice structures [102,103] and chiral domains: Since the chiral pairing state $p_b \pm ip_c$ is intrinsically degenerate, they inevitably form the chiral domain structure where the domain boundary is a pinning center of vortices. This gives rise to the complex magnetization process of this superconductor [104]. Also, it is interesting to see the chiral-nonchiral transition in the vortex lattice state under external fields [105].

There are several outstanding problems to be investigated in the future, such as the pairing mechanism leading to the present nonunitary state where longitudinal spin fluctuations are plausible. As a next step, microscopic theory and detailed calculations are definitely needed beyond the present GL framework where the most simplified version is adopted in order to just illustrate the essential points. For example, we did not seriously attempt to produce the observed H_{c2} curves quantitatively because of the reasons mentioned at the beginning of Sec. V. Thus, we only scratched its surface admittedly. It is our hope that the present theory motivates ingenious experiments in this fruitful and flourishing research field.

ACKNOWLEDGMENTS

The author is grateful for the enlightening discussions with Y. Shimizu, Y. Tokunaga, A. Miyake, T. Sakakibara, S. Nakamura, S. Kittaka, G. Knebel, A. Huxley, and K. Ishida. He would especially like to thank D. Aoki for sharing data prior to publication and stimulating discussions. He thanks K. Suzuki for helping to prepare the figures. This work is supported by JSPS KAKENHI, Grant No.17K05553.

[1] K. Machida and T. Matsubara, Spin density wave and superconductivity in highly anisotropic materials. II. Detailed study of phase transitions, J. Phys. Soc. Jpn. **50**, 3231 (1981).

[2] K. Machida and M. Kato, Inherent Spin-Density Instability in Heavy-Fermion Superconductivity, Phys. Rev. Lett. **58**, 1986 (1987).

[3] M. Kato and K. Machida, Superconductivity and spin-density waves–Application to heavy-Fermion materials, Phys. Rev. B **37**, 1510 (1988).

[4] E. Fradkin, S. A. Kivelson, and J. M. Tranquada, Theory of intertwined orders in high temperature superconductors, Rev. Mod. Phys. **87**, 457 (2015).

[5] D. Aoki, K. Ishida, and J. Flouquet, Review of U-based Ferromagnetic Superconductors: Comparison between UGe_2, URhGe, and UCoGe, J. Phys. Soc. Jpn. **88**, 022001 (2019).

[6] S. S. Saxena, P. Agarwal, K. Ahilan, F. M. Grosche, R. K. W. Haselwimmer, M. J. Steiner, E. Pugh, I. R. Walker, S. R. Julian, P. Monthoux, G. G. Lonzarich, A. Huxley, I. Sheikin, D. Braithwaite, and J. Flouquet, Superconductivity on the border of itinerant-electron ferromagnetism in UGe_2, Nature (London) **406**, 587 (2000).

[7] D. Aoki, A. Huxley, E. Ressouche, D. Braithwaite, J. Flouquet, J.-P. Brison, E. Lhotel, and C. Paulsen, Coexistence of superconductivity and ferromagnetism in URhGe, Nature (London) **413**, 613 (2001).

[8] N. T. Huy, A. Gasparini, D. E. de Nijs, Y. Huang, J. C. P. Klaasse, T. Gortenmulder, A. de Visser, A. Hamann, T. Görlach, and H. v. Löhneysen, Superconductivity on the Border of Weak Itinerant Ferromagnetism in UCoGe, Phys. Rev. Lett. **99**, 067006 (2007).

[9] S. Ran, C. Eckberg, Q.-P. Ding, Y. Furukawa, T. Metz, S. H. Saha, I.-L. Liu, M. Zie, H. Kim, J. Paglione, and N. P. Butch, Nearly ferromagnetic spin-triplet superconductivity, Science **365**, 684 (2019).

[10] D. Aoki, A. Nakamura, F. Honda, D. Li, Y. Homma, Y. Shimizu, Y. J. Sato, G. Knebel, J. P. Brison, A. Pourret, D. Braithwaite, G. Lapertot, Q. Niu, M. Vališka, H. Harima, and J. Flouquet, Unconventional superconductivity in heavy Fermion UTe_2, J. Phys. Soc. Jpn. **88**, 043702 (2019).

[11] K. Machida, Coexistence problem of magnetism and superconductivity, Appl. Phys. **35**, 193 (1984).

[12] G. Knebel, W. Knafo, A. Pourret, Q. Niu, M. Vališka, D. Braithwaite, G. Lapertot, M. Nardone, A. Zitouni, S. Mishra, I. Sheikin, G. Seyfarth, J.-P. Brison, D. Aoki, and J. Flouquet, Field-reentrant superconductivity close to a metamagnetic transition in the heavy-fermion superconductor UTe_2, J. Phys. Soc. Jpn. **88**, 063707 (2019).

[13] D. Braithwaite, M. Vališka, G. Knebel, G. Lapertot, J.-P. Brison, A. Pourret, M. E. Zhitomirsky, J. Flouquet, F. Honda, and D. Aoki, Multiple superconducting phases in a nearly ferromagnetic system, Commun. Phys. **2**, 147 (2019).

[14] A. Miyake, Y. Shimizu, Y. J. Sato, D. Li, A. Nakamura, Y. Homma, F. Honda, J. Flouquet, M. Tokunaga, and D. Aoki, Metamagneitc transition in heavy Fermion superconductor UTe_2, J. Phys. Soc. Jpn. **88**, 063706 (2019).

[15] S. Ran, I.-L. Liu, Y. S. Eo, D. J. Campbell, P. Neves, W. T. Fuhrman, S. R. Saha, C. Eckberg, H. Kim, J. Paglione, D. Graf, J. Singleton, and N. P. Butch, Extreme magnetic field-boosted superconductivity, Nat. Phys. **15**, 1250 (2019).

[16] T. Metz, S. Bao, S. Ran, I.-Lin Liu, Y. S. Eo, and W. T. Fuhrman, D. F. Agterberg, S. Anlage, N. P. Butch, and J. Paglione, Point node gap structure of spin-triplet superconductor UTe_2, Phys. Rev. B **100**, 220504(R) (2019).

[17] L. Jiao, Z. Wang, S. Ran, J. O. Rodriguez, M. Sigrist, Z. Wang, N. Butch, and V. Madhavan, Microscopic evidence for a chiral superconducting order parameter in the heavy fermion superconductor UTe_2, Nature (London) **579**, 523 (2020).

[18] Y. Tokunaga, H. Sakai, S. Kambe, T. Hattori, N. Higa, G. Nakamine, S. Kitagawa, K. Ishida, A. Nakamura, Y. Shimizu, Y. Homma, D. Li, F. Honda, and D. Aoki, ^{125}Te-NMR study on a single crystal of heavy fermion superconductor UTe_2, J. Phys. Soc. Jpn. **88**, 073701 (2019).

[19] S. Sundar, S. Gheidi, K. Akintola, A. M. Côté, S. R. Dunsiger, S. Ran, N. P. Butch, S. R. Saha, J. Paglione, and J. E. Sonier, Coexistence of ferromagnetic fluctuations and superconductivity in the actinide superconductor UTe_2, Phys. Rev. B **100**, 140502(R) (2019).

[20] G. Nakamine, S. Kitagawa, K. Ishida, Y. Tokunaga, H. Sakai, S. Kambe, A. Nakamura, Y. Shimizu, Y. Homma, D. Li, F. Honda, and D. Aoki, Superconducting properties of heavy fermion UTe_2 revealed by ^{125}Te-nuclear magnetic resonance, J. Phys. Soc. Jpn. **88**, 113703 (2019).

[21] I. M. Hayes, D. S. Wei, T. Metz, J. Zhang, Y. S. Eo, S. Ran, S. R. Saha, J. Collini, N. P. Butch, D. F. Agterberg, A. Kapitulnik, and J. Paglione, Weyl superconductivity in UTe_2, arXiv:2002.02539.

[22] S. Bae, H. Kim, S. Ran, Y. S. Eo, I.-L. Liu, W. Fuhrman, J. Paglione, N. P. Butch, and S. Anlage, Anomalous normal fluid response in a chiral superconductor, Nat. Commun. **12**, 2644 (2021).

[23] S. Ran, H. Kim, I.-L. Liu, S. Saha, I. Hayes, T. Metz, Y. S. Eo, J. Paglione, and N. P. Butch, Enhanced spin triplet superconductivity due to Kondo destabilization, Phys. Rev. B **101**, 140503 (2020).

[24] Q. Niu, G. Knebel, D. Braithwaite, D. Aoki, G. Lapertot, G. Seyfarth, J.-P. Brison, J. Flouquet, and A. Pourret, Fermi-Surface Instabilities in the Heavy-Fermion Superconductor UTe_2, Phys. Rev. Lett. **124**, 086601 (2020).

[25] V. Hutanu, H. Deng, S. Ran, W. T. Fuhrman, H. Thoma, and N. P. Butch, Crystal structure of the unconventional spin-triplet superconductor UTe_2 at low temperature by single crystal neutron diffraction, Acta Cryst. B **76**, 137 (2020).

[26] S. M. Thomas, F. B. Santos, M. H. Christensen, T. Asaba, F. Ronning, J. D. Thompson, E. D. Bauer, R. M. Fernandes, G. Fabbris, and P. F. S. Rosa, Evidence for a pressure-induced antiferromagnetic quantum critical point in intermediate valence UTe_2, Sci. Adv. **6**, eabc8709 (2020).

[27] L. P. Cairns, C. R. Stevens, C. D. O'Neill, and A. Huxley, Composition dependence of the superconducting properties of UTe_2, J. Phys.: Condens. Matter **32**, 415602 (2020).

[28] D. Aoki, F. Honda, G. Knebel, D. Braithwaite, A. Nakamura, D. Li, Y. Homma, Y. Shimizu, Y. J. Sato, J.-P. Brison, and J. Flouquet, Multiple superconducting phases and unusual enhancement of the upper critical field in UTe_2, J. Phys. Soc. Jpn. **89**, 053705 (2020).

[29] S. Kittaka, Y. Shimizu, T. Sakakibara, A. Nakamura, D. Li, Y. Homma, F. Honda, D. Aoki, and K. Machida, Orientation of point nodes and nonunitary triplet pairing tuned by the easy-axis magnetization in UTe_2, Phys. Rev. Res. **2**, 032014(R) (2020).

[30] Y. Xu, Y. Sheng, and Y. F. Yang, Quasi-Two-Dimensional Fermi Surfaces and Unitary Spin-Triplet Pairing in the Heavy Fermion Superconductor UTe_2, Phys. Rev. Lett. **123**, 217002 (2019).

[31] J. Ishizuka, S. Sumita, A. Daido, and Y. Yanase, Insulator-Metal Transition and Topological Superconductivity in UTe_2 from a First -Principles Calculation, Phys. Rev. Lett. **123**, 217001 (2019).

[32] A. B. Shick and W. E. Pickett, Spin-orbit coupling induced degeneracy in the anisotropic unconventional superconductor UTe_2, Phys. Rev. B **100**, 134502 (2019).

[33] A. H. Nevidomskyy, Stability of a nonunitary triplet pairing on the border of magnetism in UTe_2, arXiv:2001.02699.

[34] M. Fidrysiak, D. Goc-Jagło, E. Kadzielawa-Major, P. Kubiczek, and J. Spałek, Coexistent spin-triplet superconducting and ferromagnetic phases induced by Hund's rule coupling and electronic correlations: Effect of the applied magnetic field, Phys. Rev. B **99**, 205106 (2019).

[35] V. Yarzhemsky and E. A. Teplyakov, Time-reversal symmetry and the structure of superconducting order parameter of nearly ferromagnetic spin-triplet superconductor UTe_2, arXiv:2001.02963.

[36] K. Hiranuma and S. Fujimoto, Paramagnetic effects of j-electron superconductivity and application to UTe_2, J. Phys. Soc. Jpn. **90**, 034707 (2021).

[37] A. G. Lebed, Restoration of superconductivity in high magnetic fields in UTe_2, Mod. Phys. Lett. **34**, 2030007 (2020).

[38] K. Miyake, On sharp enhancement of effective mass of quasiparticles and coefficient of T^2 term of resistivity around first-order metamagnetic transition observed in UTe_2, J. Phys. Soc. Jpn. **90**, 024701 (2021).

[39] F. Lévy, I. Sheikin, B. Greinier, and A. D. Huxley, Magnetic field-induced superconductivity in the ferromagnet URhGe, Science **309**, 1343 (2005).

[40] D. Aoki, T. D. Matsuda, V. Taufour, E. Hassinger, G. Knebel, and J. Flouquet, Extremely large and anisotropic upper critical field and the ferromagnetic instability in UCoGe, J. Phys. Soc. Jpn. **78**, 113709 (2009).

[41] M. Manago, S. Kitagawa, K. Ishida, K. Deguchi, N. K. Sato, and T. Yamamura, Superconductivity at the pressure-induced ferromagnetic critical region in UCoGe, J. Phys. Soc. Jpn. **88**, 113704 (2019).

[42] M. Manago (private communication).

[43] A. J. Leggett, A theoretical description of the new phases of liquid ^{3}He, Rev. Mod. Phys. **47**, 331 (1975).

[44] W. P. Halperin, C. N. Archie, F. B. Rasmussen, T. A. Alvesalo, and R. C. Richardson, Specific heat of normal and superfluid ^{3}He on the melting curve, Phys. Rev. B **13**, 2124 (1976).

[45] V. Ambegaokar and N. D. Mermin, Thermal Anomalies of He^3: Pairing in a Magnetic Field, Phys. Rev. Lett. **30**, 81 (1973).

[46] K. Machida and T. Ohmi, Phenomenological Theory of Ferromagnetic Superconductivity, Phys. Rev. Lett. **86**, 850 (2001).

[47] Masa-aki Ozaki, K. Machida, and T. Ohmi, On p-wave pairing superconductivity under cubic symmetry, Prog. Theor. Phys. **74**, 221 (1985).

[48] Masa-aki Ozaki, K. Machida, and T. Ohmi, On p-wave pairing superconductivity under hexagonal and tetragonal symmetries, Prog. Theor. Phys. **75**, 442 (1986).

[49] T. Ohmi and K. Machida, Non-Unitary Superconducting State in UPt_3, Phys. Rev. Lett. **71**, 625 (1993).

[50] K. Machida and T. Ohmi, Identification of nonunitary triplet pairing in a heavy Fermion superconductor UPt_3, J. Phys. Soc. Jpn. **67**, 1122 (1998).

[51] A. D. Hillier, J. Quintanilla, B. Mazidian, J. F. Annett, and R. Cywinski, Nonunitary Triplet Pairing in the Centrosymmetric Superconductor $LaNiGa_2$, Phys. Rev. Lett. **109**, 097001 (2012).

[52] K. Machida, Theory of spin-polarized superconductors–an analogue of superfluid ^{3}He A-phase, J. Phys. Soc. Jpn. **89**, 033702 (2020).

[53] K. Machida, Notes on multiple superconducting phases in UTe_2, third transition, J. Phys. Soc. Jpn. **89**, 065001 (2020).

[54] G. Nakamine, K. Kinjo, S. Kitagawa, K. Ishida, Y. Tokunaga, H. Sakai, S. Kambe, A. Nakamura, Y. Shimizu, Y. Homma, D. Li, F. Honda, and D. Aoki, Anisotropic response of spin susceptibility in the superconducting state of UTe_2 probed with ^{125}Te-NMR measurement, Phys. Rev. B **103**, L100503 (2021).

[55] G. Nakamine, K. Kinjo, S. Kitagawa, K. Ishida, Y. Tokunaga, H. Sakai, S. Kambe, A. Nakamura, Y. Shimizu, Y. Homma, D. Li, F. Honda, and D. Aoki, Inhomogeneous superconducting state probed by ^{125}Te NMR on UTe_2, J. Phys. Soc. Jpn. **90**, 064709 (2021).

[56] J. F. Annett, Symmetry of the order parameter for high-temperature superconductivity, Adv. Phys. **39**, 83 (1990).

[57] K. Machida, T. Ohmi, and M. Ozaki, Anisotropy of upper critical fields for d- and p-wave pairing superconductivity, J. Phys. Soc. Jpn. **54**, 1552 (1985).

[58] K. Machida, M. Ozaki, and T. Ohmi, Unconventional superconducting class in a heavy fermion system UPt_3, J. Phys. Soc. Jpn. **59**, 1397 (1990).

[59] K. Machida, T. Fujita, and T. Ohmi, Vortex structures in an anisotropic pairing superconducting state with odd-parity, J. Phys. Soc. Jpn. **62**, 680 (1993).

[60] K. Machida, T. Nishira, and T. Ohmi, Orbital symmetry of a triplet pairing in a heavy fermion superconductor UPt_3, J. Phys. Soc. Jpn. **68**, 3364 (1999).

[61] W. Knafo, T. D. Matsuda, D. Aoki, F. Hardy, G. W. Scheerer, G. Ballon, M. Nardone, A. Zitouni, C. Meingast, and J. Flouquet, High-field moment polarization in the ferromagnetic superconductor UCoGe, Phys. Rev. B **86**, 184416 (2012).

[62] B. Wu, G. Bastien, M. Taupin, C. Paulsen, L. Howard, D. Aoki, and J.-P. Brison, Pairing mechanism in the ferromagnetic superconductor UCoGe, Nat. Commun. **8**, 14480 (2017).

[63] N. R. Werthamer, E. Helfand, and P. C. Hohenberg, Temperature and purity dependence of the superconducting critical field, H_{c2}. III. Electron spin and spin-orbit effects, Phys. Rev. **147**, 295 (1966).

[64] F. Hardy, D. Aoki, C. Meingast, P. Schweiss, P. Burger, H. v. Löhneysen, and J. Flouquet, Transverse and longitudinal magnetic-field responses in the Ising ferromagnets URhGe, UCoGe, and UGe_2, Phys. Rev. B **83**, 195107 (2011).

[65] V. P. Mineev, Reentrant superconductivity in URhGe, Phys. Rev. B **91**, 014506 (2015).

[66] E. P. Wohlfarth and P. Rhodes, Collective electron metamagnetism, Philos. Mag. **7**, 1817 (1962).

[67] M. Shimizu, Itinerant electron magnetism, J. Phys. (Paris) **43**, 155 (1982).

[68] H. Yamada, Metamagnetic transition and susceptibility maximum in an itinerant-electron system, Phys. Rev. B **47**, 11211 (1993).

[69] S. Nakamura, T. Sakakibara, Y. Shimizu, S. Kittaka, Y. Kono, Y. Haga, J. Pospíšil, and E. Yamamoto, Wing structure in the phase diagram of the Ising ferromagnet URhGe close to its tricritical point investigated by angle-resolved magnetization measurements, Phys. Rev. B **96**, 094411 (2017).

[70] D. Aoki (private communication).

[71] F. Lévy, I. Sheikin, B. Greinier, C. Marcenat, and A. D. Huxley, Coexistence and interplay of superconductivity and ferromagnetism in URhGe, J. Phys.: Condens. Matter **21**, 164211 (2009).

[72] A. Miyake (private communication).

[73] B. Wu, D. Aoki, and J.-P. Brison, Vortex liquid phase in the *p*-wave ferromagnetic superconductor UCoGe, Phys. Rev. B **98**, 024517 (2018).

[74] A. Miyake, D. Aoki, and J. Flouquet, Pressure evolution of the ferromagnetic and field re-entrant superconductivity in URhGe, J. Phys. Soc. Jpn. **78**, 063703 (2009).

[75] D. Braithwaite, D. Aoki, J.-P. Brison, J. Flouquet, G. Knebel, A. Nakamura, and A. Pourret, Dimensionality Driven Enhancement of Ferromagnetic Superconductivity in URhGe, Phys. Rev. Lett. **120**, 037001 (2018).

[76] M. Taupin, L. Howald, D. Aoki, and J.-P. Brison, Superconducting gap of UGeCo probed by thermal transport, Phys. Rev. B **90**, 180501(R) (2014).

[77] G. Knebel (private communication).

[78] S. K. Yip, T. Li, and P. Kumar, Thermodynamic considerations and the phase diagram of superconducting UPt_3, Phys. Rev. B **43**, 2742 (1991).

[79] T. Mizushima, Y. Tsutsumi, T. Kawakami, M. Sato, M. Ichioka, and K. Machida, Symmetry-protected topological superfluids and superconductors–From the basics to ^{3}He–, J. Phys. Soc. Jpn. **85**, 022001 (2016).

[80] T. Mizushima, Y. Tsutsumi, M. Sato, and K. Machida, Symmetry protected topological superfluid He^3-B, J. Phys.: Condens. Matter **27**, 113203 (2015).

[81] G. Aeppli, E. Bucher, C. Broholm, J. K. Kjems, J. Baumann, and J. Hufnagl, Magnetic Order and Fluctuations in Superconducting UPt_3, Phys. Rev. Lett. **60**, 615 (1988).

[82] T. Trappmann, H. v. Löhneysen, and L. Taillefer, Pressure dependence of the superconducting phases in UPt_3, Phys. Rev. B **43**, 13714(R) (1991).

[83] K. Machida and M. A. Ozaki, Superconducting Double Transition in A Heavy-Fermion Material UPt_3, Phys. Rev. Lett. **66**, 3293 (1991).

[84] J. A. Sauls, The order parameter for the superconducting phases of UPt_3, Adv. Phys. **43**, 113 (1993).

[85] D. Fay and J. Appel, Coexistence of p-state superconductivity and itinerant ferromagnetism, Phys. Rev. B **22**, 3173 (1980).

[86] P. Miranović, N. Nakai, M. Ichioka, and K. Machida, Orientational field dependence of low-lying excitations in the mixed state of unconventional superconductors, Phys. Rev. B **68**, 052501 (2003).

[87] Y. Tsutsumi, M. Ishikawa, T. Kawakami, T. Mizushima, M. Sato, M. Ichioka, and K. Machida, UPt_3 as a topological crystalline superconductor, J. Phys. Soc. Jpn. **82**, 113707 (2013).

[88] R. Matsuki, H. Matsuno, H. Kotegawa, H. Tou, Y. Haga, E. Yamamoto, and Y. Onuki, Study on anisotropic NMR shift in superconducting mixed state of heavy superconductor UBe_{13}, presented in Japan Physical Society Meeting on March 12, 2021 (12aH-12) (unpublished).

[89] J. F. Annett, B. L. Györffy, G. Litak, and K. I. Wysokiński, Magnetic field induced rotation of the d-vector in the spin-triplet superconductor Sr_2RuO_4, Phys. Rev. B **78**, 054511 (2008).

[90] J. F. Annett, G. Litak, B. L. Györffy, and K. I. Wysokiński, Magnetic field induced rotation of the d-vector in the spin-triplet superconductor Sr_2RuO_4, Physica C **460-462**, 995 (2007).

[91] P. Gentile, M. Cuoco, A. Romano, C. Noce, D. Manske, and P. M. R. Brydon, Spin-Orbital Coupling in a Triplet Superconductor-Ferromagnet Junction, Phys. Rev. Lett. **111**, 097003 (2013).

[92] T. Hyart, A. R. Wright, and B. Rosenow, Zeeman-field-induced topological phase transitions in triplet superconductors, Phys. Rev. B **90**, 064507 (2014).

[93] M. T. Mercaldo, M. Cuoco, and P. Kotetes, Magnetic-field-induced topological reorganization of a p-wave superconductor, Phys. Rev. B **94**, 140503(R) (2016).

[94] P. M. R. Brydon, Y. Asano, and C. Timm, Spin Josephson effect with a single superconductor, Phys. Rev. B **83**, 180504(R) (2011).

[95] H. Tou, Y. Kitaoka, K. Ishida, K. Asayama, N. Kimura, Y. Onuki, E. Yamamoto, Y. Haga, and K. Maezawa, Nonunitary Spin-Triplet Superconductivity in UPt_3: Evidence from ^{195}Pt Knight Shift Study, Phys. Rev. Lett. **80**, 3129 (1998).

[96] Y. Tsutsumi, T. Mizushima, M. Ichioka, and K. Machida, Majorana edge modes of superfluid ^{3}He A-phase in a slab, J. Phys. Soc. Jpn. **79**, 113601 (2010).

[97] Y. Tsutsumi, M. Ichioka, and K. Machida, Majorana surface states of superfluid ^{3}He A and B phases in a slab, Phys. Rev. B **83**, 094510 (2011).

[98] G. E. Volovik, Fermion zero modes on vortices in chiral superconductors, JETP Lett. **70**, 609 (1999).

[99] T. Kawakami, Y. Tsutsumi, and K. Machida, Stability of a half-quantum vortex in rotating superfluid ^{3}He-A between parallel plates, Phys. Rev. B **79**, 092506 (2009).

[100] V. Vakaryuk and A. J. Leggett, Spin Polarization of Half-Quantum Vortex in Systems with Equal Spin Pairing, Phys. Rev. Lett. **103**, 057003 (2009).

[101] M. Ichioka, T. Mizushima, and K. Machida, Skyrmion lattice and intrinsic momentum effect in the A phase of superfluid ^{3}He under rotation, Phys. Rev. B **82**, 094516 (2010).

[102] M. Takigawa, M. Ichioka, K. Machida, and M. Sigrist, Vortex structure in chiral p-wave superconductors, Phys. Rev. B **63**, 014508 (2000).

[103] M. Ichioka and K. Machida, Field dependence of the vortex structure in chiral p-wave superconductors, Phys. Rev. B **65**, 224517 (2002).

[104] M. Ichioka, Y. Matsunaga, and K. Machida, Magnetization process in a chiral p-wave superconductor with multidomains, Phys. Rev. B **71**, 172510 (2005).

[105] M. Ishihara, Y. Amano, M. Ichioka, and K. Machida, Transverse magnetic field and chiral-nonchiral transition in vortex states for nearly $B \parallel ab$ in chiral p-wave superconductors, Phys. Rev. B **87**, 224509 (2013).